

# Human occupation of northern Australia by 65,000 years ago

Chris Clarkson<sup>1</sup>, Zenobia Jacobs<sup>2,3</sup>, Ben Marwick<sup>3,4</sup>, Richard Fullagar<sup>3</sup>, Lynley Wallis<sup>5</sup>, Mike Smith<sup>6</sup>, Richard G. Roberts<sup>2,3</sup>, Elspeth Hayes<sup>3</sup>, Kelsey Lowe<sup>1</sup>, Xavier Carah<sup>1</sup>, S. Anna Florin<sup>1</sup>, Jessica McNeil<sup>1,7</sup>, Delyth Cox<sup>1</sup>, Lee J. Arnold<sup>8</sup>, Quan Hua<sup>9</sup>, Jillian Huntley<sup>10</sup>, Helen E. A. Brand<sup>11</sup>, Tiina Manne<sup>1</sup>, Andrew Fairbairn<sup>1</sup>, James Shulmeister<sup>12</sup>, Lindsey Lyle<sup>4</sup>, Makiah Salinas<sup>4</sup>, Mara Page<sup>4</sup>, Kate Connell<sup>1</sup>, Gayoung Park<sup>4</sup>, Kasih Norman<sup>1</sup>, Tessa Murphy<sup>4</sup> & Colin Pardoe<sup>13</sup>

**The time of arrival of people in Australia is an unresolved question. It is relevant to debates about when modern humans first dispersed out of Africa and when their descendants incorporated genetic material from Neanderthals, Denisovans and possibly other hominins. Humans have also been implicated in the extinction of Australia's megafauna. Here we report the results of new excavations conducted at Madjedbebe, a rock shelter in northern Australia. Artefacts in primary depositional context are concentrated in three dense bands, with the stratigraphic integrity of the deposit demonstrated by artefact refits and by optical dating and other analyses of the sediments. Human occupation began around 65,000 years ago, with a distinctive stone tool assemblage including grinding stones, ground ochres, reflective additives and ground-edge hatchet heads. This evidence sets a new minimum age for the arrival of humans in Australia, the dispersal of modern humans out of Africa, and the subsequent interactions of modern humans with Neanderthals and Denisovans.**

The date when humans first arrived in Sahul—the combined Pleistocene landmass of Australia and New Guinea—remains a contested issue. Resolving this question has important implications for debates about the timing and rate of dispersal of modern humans out of Africa and across south Asia<sup>1–3</sup>, and when and where genetic material was transferred between archaic hominins and modern humans<sup>4–7</sup>. The impact of humans on Australia's ecosystems has also been a long-standing topic of discussion<sup>8–12</sup>.

Current estimates of the time of initial human colonization of Australia range from 47 thousand years ago (ka) to around 60 ka (refs 9, 12–23). A key site in this debate is Madjedbebe, a rock shelter in northern Australia formerly known as Malakunanja II, which was excavated in 1973 (ref. 24) and 1989 (ref. 13). The earliest artefacts recovered from the latter excavation included stone tools and ground ochre pieces deposited between about 60 and 50 ka, based on thermoluminescence and optical (optically stimulated luminescence, OSL) dating of the surrounding sediments<sup>13,16</sup>. These ages, the depositional context of the artefacts and their significance have proved contentious, mainly because of the lack of detailed description of the artefacts and concerns over stratigraphic disturbance of the deposit and how the artefacts relate to the dated sediments<sup>19–22,25–30</sup>. Here we report the results of new excavations at Madjedbebe, concentrating on evidence regarding the age and stratigraphic integrity of the deposits and associated artefacts in the zone of initial human occupation.

## Excavations and stratigraphy

Madjedbebe rock shelter is located on the western edge of the Arnhem Land plateau in the Northern Territory, in Mirarr Country (12° 30' S, 132° 53' E, approximately 20 m above sea level; Fig. 1a, b and Extended

Data Fig. 1b, c). The 1989 excavation<sup>13</sup> revealed cultural deposits starting at 2.6 m depth below the surface, with a peak in artefact density at 2.5–2.3 m depth below surface. Silcrete flakes, ground ochre, a grindstone and more than 1,500 stone artefacts were recovered from the lowest occupation levels<sup>22</sup>. The associated sediments were dated to around 60–50 ka using thermoluminescence methods, with total uncertainties of 16–20 thousand years (kyr) at the 95.4% confidence level<sup>15,25</sup>. These ages made Madjedbebe the oldest human occupation site known in Australia; two of these samples were subsequently dated by single-grain OSL methods, which were then under development, and these ages supported the early thermoluminescence chronology<sup>16,29,30</sup>. We conducted new excavations at Madjedbebe in 2012 and 2015 to obtain additional artefacts and sediment samples for high-resolution OSL dating from the zone of the initial occupation, in particular.

We excavated twenty 1 × 1 m squares adjacent to, and enclosing, the original excavations (Fig. 1c) to a maximum depth of 3.4 m. The three-dimensional coordinates of approximately 11,000 artefacts and other anthropogenic features (hearths, burials and pits) were recorded and samples were collected for chronological, geoarchaeological and macrobotanical analyses. We focus here on the northwest squares of the excavation (southwest faces of B4–B6 and northwest face of C4), where the frequency of artefacts and the number of OSL samples is greatest (Extended Data Fig. 1a) and refer to other squares for ancillary data.

The basal deposits consist of culturally sterile orange sands. The lowest artefacts were recovered from the overlying unit (around 0.7 m thick and composed of well-sorted medium-coarse pink sand), which dips at a low angle (around 5°) towards the front of the shelter. The upper boundary of this unit occurs at 2.0–2.5 m depth (increasing with distance from the back wall; Extended Data Fig. 1a), where it

<sup>1</sup>School of Social Science, University of Queensland, Brisbane, Queensland 4072, Australia. <sup>2</sup>Australian Research Council (ARC) Centre of Excellence for Australian Biodiversity and Heritage, University of Wollongong, Wollongong, New South Wales 2522, Australia. <sup>3</sup>Centre for Archaeological Science, School of Earth and Environmental Sciences, University of Wollongong, Wollongong, New South Wales 2522, Australia. <sup>4</sup>Department of Anthropology, University of Washington, Seattle, Washington 98195, USA. <sup>5</sup>Nulungu Research Institute, University of Notre Dame, Broome, Western Australia 6725, Australia. <sup>6</sup>Centre for Historical Research, National Museum of Australia, Canberra, Australian Capital Territory 2601, Australia. <sup>7</sup>Department of Anthropology, Harvard University, Cambridge, Massachusetts 02143, USA. <sup>8</sup>School of Physical Sciences, the Environment Institute and the Institute for Photonics and Advanced Sensing, University of Adelaide, Adelaide, South Australia 5005, Australia. <sup>9</sup>Australian Nuclear Science and Technology Organisation, Lucas Heights, New South Wales 2234, Australia. <sup>10</sup>Place, Evolution, Rock Art, Heritage Unit, School of Humanities, Griffith University, Nathan, Queensland 4222, Australia. <sup>11</sup>Australian Synchrotron, 800 Blackburn Road, Clayton, Victoria 3168, Australia. <sup>12</sup>School of Earth and Environmental Sciences, University of Queensland, Brisbane, Queensland 4072, Australia. <sup>13</sup>Archaeology and Natural History, School of Culture, History and Language, The Australian National University, Canberra, Australian Capital Territory 2601, Australia.

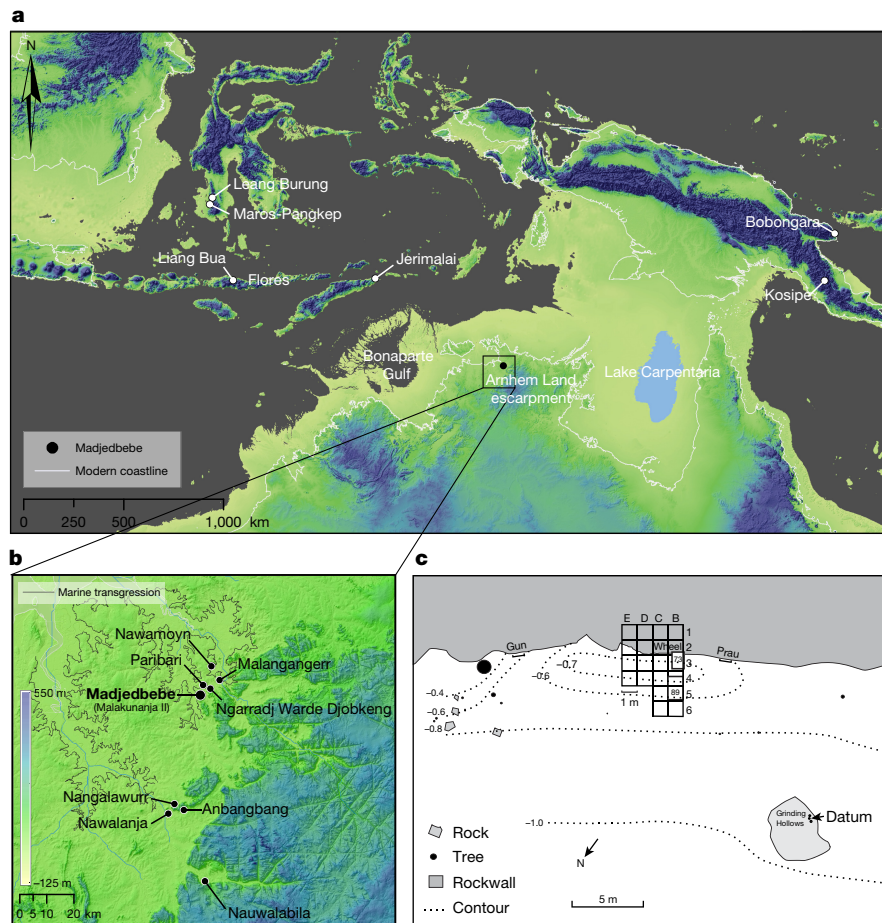


**Figure 1 | Site location and stratigraphy.** **a**, Regional map showing the location of Madjedbebe in relation to the coastline at 65 ka and the current coastline (white line), and other ancient archaeological sites in Australia and southeast Asia (bathymetric data GEBCO 2014 Grid, version 20150318, <http://www.gebco.net>). **b**, Location of Madjedbebe in relation to

other key archaeological sites in Kakadu National Park, and the location of the high sea-level stand during the last marine transgression about 6–7 ka (topographic data Geoscience Australia 1 arc-second DEM). **c**, Site plan showing the 1973, 1989, 2012 and 2015 excavation squares. Squares E1–B2 were located beneath the sloping back wall.

grades diffusely into poorly sorted medium–coarse (light) brown sands. Organic inclusions are rare, but spalled fragments of bedrock are common, especially near the dripline in square B6. No stone lines, pavements or imbricated structures were encountered during the excavation. The brown sands are compacted below about 1.5 m depth, but become softer and encrusted with carbonates closer to its diffuse contact with the overlying midden (approximately 0.5 m thick). The latter consists of brown silty sand, abundant gastropod shells, numerous bone specimens and some plant roots, and is buried beneath a loose surface layer of dark sandy silt containing abundant charcoal fragments. Most archaeofaunal remains were recovered from this Holocene midden, with some degraded bone found to a depth of 1.76 m. Midden bone is exceptionally well-preserved, including a maxillary fragment of a thylacine (*Thylacinus cynocephalus*) coated in red pigment (Fig. 2o–q).

### Artefacts and depositional integrity

Artefacts occur in three dense bands (Extended Data Figs 1, 2), with fewer artefacts in the intervening deposits. Each band corresponds to a change in raw material use and stone working technology (Extended Data Fig. 2a, b) and there is no size sorting of artefacts with depth (posterior  $r^2$  distribution, 95% credible interval: 0.0004–0.0049). These observations imply overall stratigraphic integrity of the deposit.

The lowest dense band (phase 2) at 2.60–2.15 m depth in squares B4–B6 represents the zone of first occupation; it contains an *in situ* hearth and an assemblage of distinctive stone artefacts made mostly from quartzite, silcrete, mudstone and dolerite (Fig. 2 and Extended Data Fig. 2b). The assemblage includes a number of distinctive artefact

types, such as thinning flakes and snapped points (Fig. 2c, d), faceted discoidal cores (Fig. 2h), grinding stones (Fig. 2e, f and Extended Data Fig. 3), whole and fragments of edge-ground hatchets (Fig. 2a, b and Extended Data Fig. 4), ground ochres (Fig. 2g) and fragments of sheet mica (Fig. 2k)—several of which were wrapped around a large piece of ground yellow ochre (Fig. 2k–m).

Artefact residues and macrofossil remains demonstrate exploitation of fuel wood and a range of plant foods (seeds, tubers and *Pandanus* sp. nuts; Extended Data Fig. 5b–d) from the local eucalyptus and monsoon vine thicket forest. The middle dense band (phase 4) at 1.55–0.95 m depth shows an increase in the use of bipolar technology (Extended Data Fig. 2c); quartzite is rare and quartz is abundant (Extended Data Fig. 2b). The upper dense band (0.70–0.35 m depth) is dominated by quartz and chert artefacts with single and multiplatform cores (Extended Data Fig. 2b, c).

Three lines of evidence suggest that post-depositional vertical mixing of the deposit and artefact movement is restricted to depths of approximately 10 cm. First, we refitted silcrete artefacts from the lower and middle dense bands, and found 14 and 3 refits within these two bands, respectively, but not between them (Extended Data Fig. 6); the median vertical distance between refitted pieces is 10.6 cm. The limited downward movement of artefacts is consistent with the outcome of modern trampling experiments at Madjedbebe<sup>31</sup>. Second, burnt artefacts are more abundant in these two bands—indicating a probable association with intense anthropogenic burning—than in the intervening deposits (Extended Data Fig. 7b); their vertical separation, and the presence of intact hearths, argues against mixing and stratigraphic disturbance over



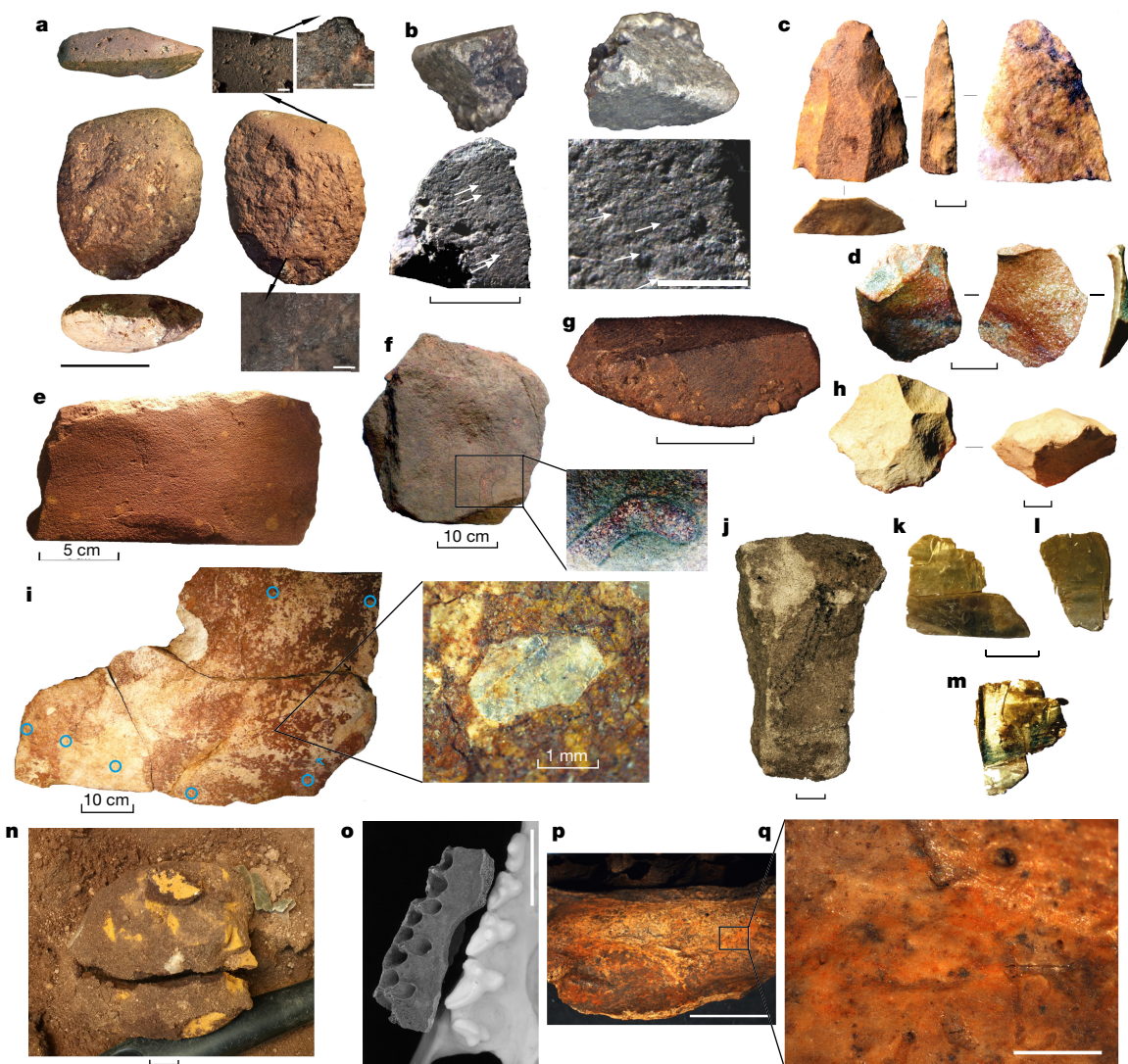


**Figure 2 | Artefacts from the 2012 and 2015 excavations.** All artefacts are from phase 2 except i (phase 3), f and j (phase 4). Scale bars are 1 cm unless indicated otherwise. **a**, Ground hatchet head number 9 from B1/36 (phase 2). Scale bar, 5 cm. Top insets and micrographs show striations and grinding (left; scale bar, 2 mm) and edge rounding and polish from use (right; scale bar, 0.2 mm). Bottom micrograph and inset show polish (scale bar, 0.2 mm) from movement inside the haft. **b**, Edge-ground margin on flake UPAF51 C2/52 (phase 2). Scale bar, 5 mm. Bottom-right inset (scale bar, 2 mm) shows striations (arrows) from use and grinding. Top-left, the ground edge is shown viewed from the side. Top-right, the ground edge is shown viewed from the front. **c**, Invasively retouched silcrete point from C6/61. **d**, Silcrete thinning flake B4/43 (1989). **e**, Sandstone grinding stone GS79 from B6/54. **f**, Mortar GS32 from B6/31, used to pound hard plant material and with possible outline motif in the bottom-right

corner. **g**, Ground ochre 'crayon' B6/52. **h**, Faceted discoidal core from C6/42. **i**, Conjoining ochre-covered slab (ART9) from D2/33; inset shows fragment of mica embedded in a thick coating of ochre, with blue circles at the <8.5-mm-diameter pXRF sampling locations. **j**, Charcoal lines and dots on sandstone piece from C2/26. **k–m**, Pieces of sheet mica from C5/56 found wrapped around a large, ground yellow ochre 'crayon' (**n**). **o–q**, Photographs of a maxillary fragment of thylacine or Tasmanian tiger (*Thylacinus cynocephalus*) from C2/9, coated in red pigment. **o**, Archaeological specimen (left) is shown relative to a modern thylacine cast. **p** and **q**, Detail of ochred surface at 6.7× magnification (scale bar, 10 mm) and 45× magnification (scale bar, 1 mm), respectively. The probable age of the thylacine specimen is 2.7–3.9 calibrated kyr BP, as indicated by  $^{14}\text{C}$  ages for spit 9 in the surrounding squares (D3 and C4).

depths of several decimetres. Third, micromorphological observations indicate only small-scale reworking of the Pleistocene deposits: sand-sized quartz grains have cappings and linked-cappings of fine silt grains (Extended Data Fig. 7f, k, l), which represent episodes of wetting and drying on stable surfaces that have been disturbed subsequently, but microfauna galleries are absent.

### Numerical chronology

We dated the deposits using radiocarbon ( $^{14}\text{C}$ ) and single-grain OSL techniques. Most of the charcoal samples are isolated fragments, which decrease in abundance with depth, but nine samples were collected from *in situ* hearths in the northwest squares (Extended Data Fig. 5a). Charcoal was pretreated using acid–base–acid or acid–base

wet-oxidation procedures (the latter preferred for charcoal older than around 20 kyr<sup>32,33</sup> and the  $^{14}\text{C}$  content measured by accelerator mass spectrometry (see Methods). The  $^{14}\text{C}$  ages of 22 charcoal samples (15 from the northwest squares) increase progressively to around 34 calibrated kyr before present (BP) at a depth of approximately 1.6 m, but some isolated fragments have stratigraphically inconsistent ages (Extended Data Fig. 8g). We attribute these anomalies to small-scale mixing of the deposits through post-depositional movement of charcoal fragments and digging of hearth pits.

OSL dating gives an estimate of the time since mineral grains were last exposed to sunlight<sup>34</sup>. We applied this method to individual grains of quartz<sup>35,36</sup> from 56 samples (44 from the northwest squares), including the measurement of four samples in two separate laboratories

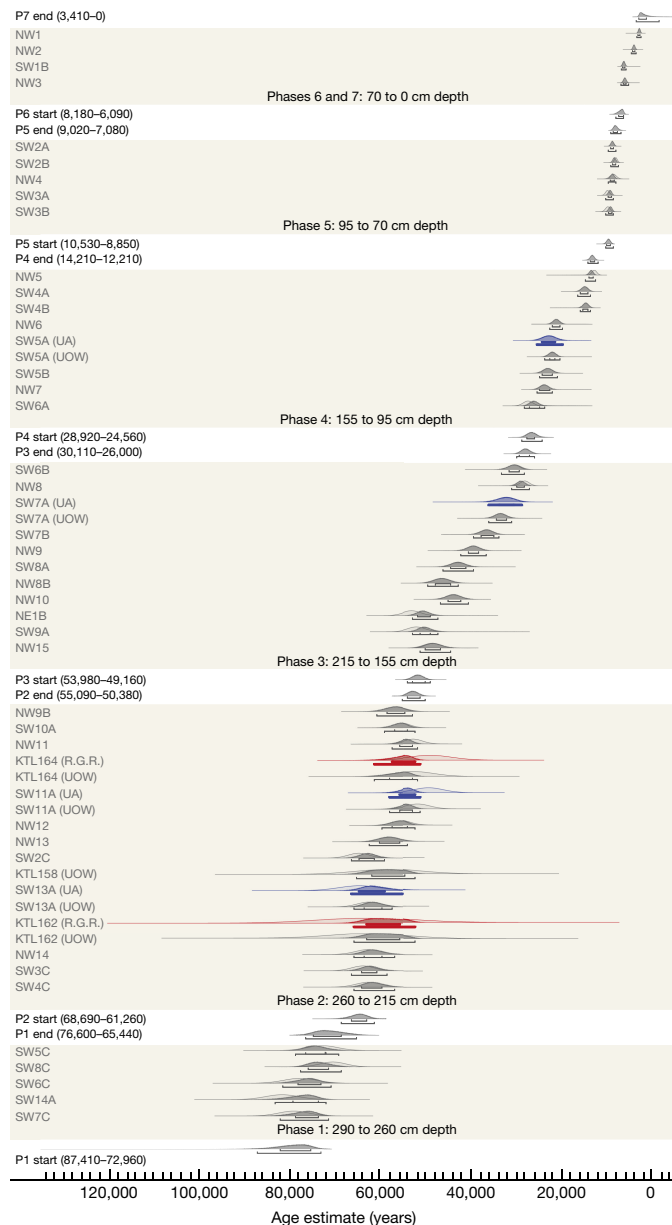


**Figure 3 | Bayesian model of the single-grain OSL ages.** Ages have been modelled in OxCal version 4.2. Only random errors are included. Pale probability distributions represent the unmodelled ages (likelihoods) and dark grey distributions represent the modelled ages (posterior probabilities) obtained in this study at the University of Wollongong (UOW). Blue distributions represent the ages obtained at the University of Adelaide (UA) for the four replicate samples in this study, while those in red (labelled R.G.R.) represent the two single-grain OSL ages reported in ref. 16. The two brackets beneath the distributions represent the 68.2% and 95.4% probability ranges. Start and end boundary ages have been modelled for each of the phases, with the age ranges (95.4% confidence interval, random-only errors) given in years and rounded off to the closest decade.

(Z.J. and L.J.A.) and four samples collected by R.G.R. in 1989 (KTL158, 162, 164 and 165)<sup>13</sup>. Many of the equivalent-dose distributions include some grains with smaller values than those of the majority of grains (Extended Data Fig. 9), which we interpret as evidence of small-scale disturbance of the deposit; some of the OSL samples were collected in 5-cm-diameter tubes, which will also result in some time-averaging (approximately 1,250 years at an average sedimentation rate of about 4 cm kyr<sup>-1</sup>; see Supplementary Information). The OSL ages show a general pattern of increasing age with depth (Fig. 3 and Extended Data Fig. 8c–f), with consistent estimates obtained for both the replicate

and 1989 samples (Extended Data Fig. 10). The ages are also in good agreement with the <sup>14</sup>C chronology (Extended Data Fig. 8g). Both chronologies support previous inferences<sup>16,22,30</sup>, and the additional lines of evidence presented above, for limited post-depositional disturbance of the Pleistocene deposits and vertical displacement of associated artefacts.

We developed a Bayesian model based on the OSL chronology (Fig. 3) to estimate the start and end ages for the three dense bands of artefacts. The lowest dense band—the zone of first occupation—has modelled mean start and end ages of 65.0 ± (3.7, 5.7) and 52.7 ± (2.4, 4.3) kyr, respectively; the first and second error terms are the modelled age uncertainties at 95.4% probability, excluding and including the total systematic error, respectively (see Supplementary Information). These ages give a mean sediment accumulation rate of 4.1 ± 0.8 cm kyr<sup>-1</sup> for the lowest dense band. The middle dense band has modelled start and end ages of 26.7 ± (2.2, 2.8) and 13.2 ± (1.0, 1.3) kyr, corresponding to a mean accumulation rate of 4.4 ± 0.4 cm kyr<sup>-1</sup>, and the upper dense band has a modelled start age of 7.1 ± (1.0, 1.1) kyr. This new chronology confirms the stratigraphic integrity of Australia's oldest known archaeological site and extends the timing of first occupation to around 65 ka, with more precise ages than those that have been obtained previously<sup>13,15,16</sup>; the total age uncertainties are only 3–4 kyr (68.2% confidence interval) for the OSL samples associated with the lowest dense band of artefacts.

## Discussion and implications

The new excavations have yielded a much larger and more diverse artefact assemblage than those reported previously<sup>13,22</sup>, with more than 10,000 artefacts recovered *in situ* from the zone of first occupation. The improved chronological resolution for the site allows firmer conclusions to be drawn about the global significance of the earliest artefacts. The first occupants used elaborate lithic technology, ochre 'crayons' and other pigments—including one of the oldest known examples in the world of the use of reflective (micaceous) pigment (Fig. 2i, k–m). They also collected and processed plant foods, as revealed by macrofossils and artefact residues. Artefacts in the lowest dense band show traces of Australia's earliest evidence of seed grinding and pigment processing, together with the world's oldest known edge-ground hatchets<sup>37,38</sup> (Fig. 2a).

The settlement of Madjedbebe around 65 ka (conservatively 59.3 ka, calculated as 65.0 ka minus the age uncertainty of 5.7 kyr at 95.4% probability) sets a new minimum age for the human colonization of Australia and the dispersal of modern humans out of Africa and across south Asia. The final stages of this journey took place at a time of lower sea level, when northern Australia was cooler and wetter. Our chronology places people in Australia more than 20 kyr before continent-wide extinction of the megafauna<sup>9–11</sup> and supports an age of more than 60 kyr for the incorporation of Neanderthal and Denisovan DNA into the modern human genome<sup>1–7</sup>. It also extends the period of overlap of modern humans and *Homo floresiensis* in eastern Indonesia to at least 15 kyr (ref. 39) and, potentially, with other archaic hominins—such as *Homo erectus*<sup>40</sup>—in southeast Asia and Australasia.

**Online Content** Methods, along with any additional Extended Data display items and Source Data, are available in the online version of the paper; references unique to these sections appear only in the online paper.

**Received 30 November 2016; accepted 19 May 2017.**

1. Mallick, S. *et al.* The Simons Genome Diversity Project: 300 genomes from 142 diverse populations. *Nature* **538**, 201–206 (2016).
2. Malaspinas, A.-S. *et al.* A genomic history of Aboriginal Australia. *Nature* **538**, 207–214 (2016).
3. Pagani, L. *et al.* Genomic analyses inform on migration events during the peopling of Eurasia. *Nature* **538**, 238–242 (2016).
4. Reich, D. *et al.* Genetic history of an archaic hominin group from Denisova Cave in Siberia. *Nature* **468**, 1053–1060 (2010).
5. Sankararaman, S., Patterson, N., Li, H., Pääbo, S. & Reich, D. The date of interbreeding between Neandertals and modern humans. *PLoS Genet.* **8**, e1002947 (2012).



6. Fu, Q. *et al.* Genome sequence of a 45,000-year-old modern human from western Siberia. *Nature* **514**, 445–449 (2014).
7. Kuhlwiilm, M. *et al.* Ancient gene flow from early modern humans into Eastern Neanderthals. *Nature* **530**, 429–433 (2016).
8. Bird, M. I. *et al.* Humans, megafauna and environmental change in tropical Australia. *J. Quat. Sci.* **28**, 439–452 (2013).
9. Saltr , F. *et al.* Climate change not to blame for late Quaternary megafauna extinctions in Australia. *Nat. Commun.* **7**, 10511 (2016).
10. Johnson, C. N. *et al.* What caused extinction of the Pleistocene megafauna of Sahul? *Proc. R. Soc. B* **283**, 20152399 (2016).
11. van der Kaars, S. *et al.* Humans rather than climate the primary cause of Pleistocene megafaunal extinction in Australia. *Nat. Commun.* **8**, 14142 (2017).
12. Hamm, G. *et al.* Cultural innovation and megafauna interaction in the early settlement of arid Australia. *Nature* **539**, 280–283 (2016).
13. Roberts, R. G., Jones, R. & Smith, M. A. Thermoluminescence dating of a 50,000-year-old human occupation site in northern Australia. *Nature* **345**, 153–156 (1990).
14. Roberts, R. G. *et al.* The human colonisation of Australia: optical dates of 53,000 and 60,000 years bracket human arrival at Deaf Adder Gorge, Northern Territory. *Quat. Sci. Rev.* **13**, 575–583 (1994).
15. Roberts, R. G. & Jones, R. Luminescence dating of sediments: new light on the human colonisation of Australia. *Aust. Aborig. Stud.* **1994**, 2–17 (1994).
16. Roberts, R. G. *et al.* Single-aliquot and single-grain optical dating confirm thermoluminescence age estimates at Malakunanja II rockshelter in northern Australia. *Anc. TL* **16**, 19–24 (1998).
17. Turney, C. S. M. *et al.* Early human occupation at Devil's Lair, southwestern Australia 50,000 years ago. *Quat. Res.* **55**, 3–13 (2001).
18. Bowler, J. M. *et al.* New ages for human occupation and climatic change at Lake Mungo, Australia. *Nature* **421**, 837–840 (2003).
19. O'Connell, J. F. & Allen, J. Dating the colonization of Sahul (Pleistocene Australia–New Guinea): a review of recent research. *J. Archaeol. Sci.* **31**, 835–853 (2004).
20. Allen, J. & O'Connell, J. F. Both half right: updating the evidence for dating first human arrivals in Sahul. *Aust. Archaeol.* **79**, 86–108 (2014).
21. O'Connell, J. F. & Allen, J. The process, biotic impact, and global implications of the human colonization of Sahul about 47,000 years ago. *J. Archaeol. Sci.* **56**, 73–84 (2015).
22. Clarkson, C. *et al.* The archaeology, chronology and stratigraphy of Madjedbebe (Malakunanja II): a site in northern Australia with early occupation. *J. Hum. Evol.* **83**, 46–64 (2015).
23. Veth, P. *et al.* Early human occupation of a maritime desert, Barrow Island, north-west Australia. *Quat. Sci. Rev.* **168**, 19–29 (2017).
24. Kamminga, J. & Allen, H. *Alligator Rivers Environmental Fact Finding Study: Report of the Archaeological Survey* (Australian Government, Canberra, 1973).
25. Roberts, R. G., Jones, R. & Smith, M. A. Stratigraphy and statistics at Malakunanja II: reply to Hiscock. *Archaeol. Ocean.* **25**, 125–129 (1990).
26. Hiscock, P. How old are the artefacts at Malakunanja II? *Archaeol. Ocean.* **25**, 122–124 (1990).
27. Bowdler, S. 50,000 year-old site in Australia—is it really that old? *Aust. Archaeol.* **31**, 93 (1990).
28. O'Connell, J. F. & Allen, J. When did humans first arrive in greater Australia and why is it important to know? *Evol. Anthropol.* **6**, 132–146 (1998).
29. Jones, R. Dating the human colonization of Australia: radiocarbon and luminescence revolutions. *Proc. Br. Acad.* **99**, 37–65 (1999).
30. Roberts, R. G. & Jones, R. in *Humanity from African Naissance to Coming Millennia: Colloquia in Human Biology and Palaeoanthropology* (eds Tobias, P. V., Raath, M. A., Moggi-Cecchi, J. & Doyle, G. A.) 239–248 (Firenze Univ. Press & Witwatersrand Univ. Press, 2001).
31. Marwick, B., Hayes, E., Clarkson, C. & Fullagar, R. Movement of lithics by trampling: an experiment in the Madjedbebe sediments, northern Australia. *J. Archaeol. Sci.* **79**, 73–85 (2017).
32. Bird, M. I. *et al.* Radiocarbon dating of “old” charcoal using a wet oxidation, stepped-combustion procedure. *Radiocarbon* **41**, 127–140 (1999).
33. Bird, M. I. *et al.* The efficiency of charcoal decontamination for radiocarbon dating by three pre-treatments — ABOX, ABA and hypy. *Quat. Geochronol.* **22**, 25–32 (2014).
34. Huntley, D. J., Godfrey-Smith, D. I. & Thewalt, M. L. W. Optical dating of sediments. *Nature* **313**, 105–107 (1985).
35. Jacobs, Z. & Roberts, R. G. Advances in optically stimulated luminescence dating of individual grains of quartz from archeological deposits. *Evol. Anthropol.* **16**, 210–223 (2007).
36. Roberts, R. G. *et al.* Optical dating in archaeology: thirty years in retrospect and grand challenges for the future. *J. Archaeol. Sci.* **56**, 41–60 (2015).
37. Geneste, J.-M. *et al.* Earliest evidence for ground-edge axes: 35,400±410 cal BP from Jayoyn Country, Arnhem Land. *Aust. Archaeol.* **71**, 66–69 (2010).
38. Hiscock, P., O'Connor, S., Balme, J. & Maloney, T. World's earliest ground-edge axe production coincides with human colonisation of Australia. *Aust. Archaeol.* **82**, 2–11 (2016).
39. Sutikna, T. *et al.* Revised stratigraphy and chronology for *Homo floresiensis* at Liang Bua in Indonesia. *Nature* **532**, 366–369 (2016).
40. Mondal, M. *et al.* Genomic analysis of Andamanese provides insights into ancient human migration into Asia and adaptation. *Nat. Genet.* **48**, 1066–1070 (2016).

**Supplementary Information** is available in the online version of the paper.

**Acknowledgements** The authors are grateful to the custodians of Madjedbebe, the Mirarr Senior Traditional Owners (Y. Margarula and M. Nango) and our research partners (Gundjeihmi Aboriginal Corporation) for permission to carry out this research and publish this paper. We are also grateful to J. O'Brien and D. Vadielloo for assistance in the field. This research was funded through Australian Research Council grants and fellowships to C.C., B.M., L.W., R.F., M.Sm. (DP110102864), B.M. (FT140100101), Z.J. (DP1092843, FT150100138), R.G.R. (FL130100116), T.Ma. (DE150101597) and L.J.A. (FT130100195), and through Australian Postgraduate Awards to X.C., E.H., S.A.F. and K.L. B.M. was also supported by a DAAD Fellowship (A/14/01370), a UW-UQ Trans-Pacific Fellowship, and UW Royalty Research Fellowship (65-4630). S.A.F. was also supported by an AINSE Postgraduate Research Award (11877) and a Wenner Gren Dissertation Fieldwork Grant (Gr.9260). Radiocarbon analyses were partly funded by Australian Institute of Nuclear Science and Engineering grants 13/003 and 15/001 to C.C., X.C., S.A.F. and K.N. We acknowledge financial support from the Australian Government's National Collaborative Research Infrastructure Strategy (NCRIS) for the Centre for Accelerator Science at the Australian Nuclear Science and Technology Organisation. A L'Or al Australia For Women in Science Fellowship to Z.J. supported the re-dating of the original sediment samples. Part of this work was undertaken on the powder diffraction beamline at the Australian Synchrotron. We thank E. Grey, R. MacPhail, S. Mentzer, C. Miller, M. Svob, and X. Villagran for assistance with geoarchaeological analysis, T. Lachlan and Y. Jafari for help with OSL dating and related illustrations, and C. Matheson and J. Field for assistance with residue analysis.

**Author Contributions** C.C., B.M., R.F., L.W. and M.Sm. obtained funding and conducted the excavation. Z.J. performed the OSL dating and Bayesian modelling. L.J.A. conducted the blind OSL dating study. Q.H. conducted <sup>14</sup>C dating. C.C. and B.M. analysed the stone artefacts. J.M. performed the refitting. B.M. and K.L. conducted geoarchaeological investigations. T.Ma. performed vertebrate faunal identification. D.C. analysed the ground ochre assemblage. R.F. and E.H. analysed the stone artefact usewear and residues. S.A.F., X.C. and A.F. analysed the archaeobotanical assemblage. K.C. performed microscopy on ART9 mica. K.N. made the map in Fig. 1 and performed analysis of marine transgression for the study region. J.H. conducted the pXRF analyses. J.H. and H.E.A.B. collected and analysed the pigment samples using synchrotron powder XRD. J.S. summarized palaeoclimate data for northern Australia. L.L., M.Sa., M.P., G.P. and T.Mu. performed isotopic and sediment analyses. C.P. performed skeletal analysis and assisted with in-field excavation processing. C.C., Z.J., B.M. and R.G.R. wrote the main text with specialist contributions from other authors.

**Author Information** Reprints and permissions information is available at [www.nature.com/reprints](http://www.nature.com/reprints). The authors declare no competing financial interests. Readers are welcome to comment on the online version of the paper. Publisher's note: Springer Nature remains neutral with regard to jurisdictional claims in published maps and institutional affiliations. Correspondence and requests for materials should be addressed to C.C. ([c.clarkson@uq.edu.au](mailto:c.clarkson@uq.edu.au)) and Z.J. ([zenobia@uow.edu.au](mailto:zenobia@uow.edu.au)).

**Reviewer Information** *Nature* thanks R. Dennell, C. Marean, E. J. Rhodes and J.-L. Schwenninger for their contribution to the peer review of this work.

## METHODS

**Excavation methods.** Excavation took place in  $1 \times 1$  m squares in 2–5 cm spits within stratigraphic layers. Twenty  $1 \times 1$  m squares were excavated adjacent to and enclosing the original 1973 and 1989 excavations (Fig. 1c). Eight squares were dug to 2.75 m depth (B1, C1–3, D1–3, E2), while five squares were dug to 3 m depth (B5, B6, C4–6) and two squares (B2, B3) to 3.4 m depth in 2012 and 2015. One square was dug to 4.3 m depth in 1989 (B4), with the remaining squares discontinued at 1.3–1.5 m depth to maintain baulks and site stability (E1, E3, E4, D4). The deeper squares were excavated in 72 spits, with spits averaging 4–5 cm deep in the upper deposit where dense shell midden was present, and averaging 2.5 cm deep from 2–3 m depth. All artefacts larger than 2 cm were piece-plotted *in situ* with a total station and bagged separately with a unique identifying number. Artefacts were identified during the excavation, where possible, and coded by type (lithic, haematite, bone, human bone, axe, axe flake, grinding stone, and so on). Sedimentary features (abbreviated as SF) were outlined and contours plotted with a total station. The latter included human burial cuts, hearths, pits and intrusive features such as root casts, burrows and postholes. All sediments were passed through nested 3 and 7 mm mesh sieves and a 100 g sediment sample was retained from each spit. Munsell colour and pH values were obtained for each spit and all sieve residue was bagged and transported to the University of Queensland archaeology laboratories for sorting. Sediments were extensively sampled for pollen, geoarchaeology and phytoliths, and blocks were taken from the walls for soil micromorphology. Bulk sediment samples were also collected from two columns (see 'Archaeobotanical analysis methods'). The site was backfilled with the original sediment and all human bone was reinterred after analysis at the completion of the excavation in 2016.

**Artefact analysis methods.** All stone artefacts were counted and weighed according to raw material, artefact type (core, flake, retouched flake, flaked piece) and typology. A complete list is provided in the Supplementary Information for select squares. The number of artefacts per spit was divided by litres excavated to calculate artefact frequencies (density per spit). Plotted artefacts were left unwashed. Heat-affected artefacts were identified by high lustre, crenated fracture, crazing, irregular heat-exfoliation surfaces and pot-lid scarring. Ground and retouched artefacts were initially inspected under low magnification and selected items were analysed for functional traces, including usewear and residues. Haematite pieces were classified as ground and unground, and counted and weighed. Ground haematite was analysed in detail for the number of ground facets, quality and colour, and selected pieces were further analysed under high magnification for usewear and residues.

**Radiocarbon dating of charcoal.** Charcoal samples were submitted for analysis to two different radiocarbon laboratories—Waikato (Wk) and ANSTO (OZ) in New Zealand and Australia, respectively. Samples were collected during the 2012 and 2015 excavation seasons and were carefully recorded and plotted using a total station. The samples were collected from a number of different squares (B3–E3, C4, C5 and E4). The relevant squares are shaded in grey in Extended Data Fig. 8a and the sample codes, contexts and chemical pretreatments are provided in Supplementary Table 2. Samples were taken from depths of between 8 cm and 200 cm below the ground surface.

Samples submitted to Waikato were first physically cleaned of any adhering sediment and loose material, and then crushed. This was followed by an acid–base–acid (ABA) chemical pretreatment, in which samples were washed in hot HCl, rinsed, treated with NaOH and rinsed again, and then treated with hot HCl, rinsed and dried. The pretreated samples were then combusted to  $\text{CO}_2$  by oxidation at  $800^\circ\text{C}$  using CuO. The  $\text{CO}_2$  was purified in the presence of silver wire to absorb any  $\text{SO}_x$  and  $\text{NO}_x$  produced. The  $\text{CO}_2$  was then reduced to graphite with  $\text{H}_2$  at  $550^\circ\text{C}$  using an iron catalyst. The pressed graphite targets were sent to the Keck Radiocarbon Dating Laboratory at the University of California, Irvine and the Center for Applied Isotope Studies, University of Georgia for accelerator mass spectrometry (AMS) measurements.

Samples submitted to ANSTO were pretreated using either the ABA procedure (for samples younger than around 20 kyr) or the acid–base wet-oxidation (ABOX) procedure (for samples older than around 20 kyr). The ABOX pretreatment included washes in acid (2 M HCl at  $60^\circ\text{C}$  for 2 h), alkali (1% NaOH at  $60^\circ\text{C}$  for 1 h) and acid (0.1 M  $\text{K}_2\text{Cr}_2\text{O}_7$  at  $60^\circ\text{C}$  for 24 h), with Milli-Q water rinses between each step or until the solutions were clear. The pretreated samples were oven-dried at  $60^\circ\text{C}$  for two days before being combusted to  $\text{CO}_2$  using the sealed-tube technique, after which the  $\text{CO}_2$  was reduced to graphite using the  $\text{H}_2/\text{Fe}$  method<sup>41</sup>. A portion of graphite was used to determine the  $\delta^{13}\text{C}$  value, for the isotopic fractionation correction, using a Vario Microcube elemental analyser and an IsoPrime isotope-ratio mass spectrometer. AMS measurements of  $^{14}\text{C}$  content were carried out using the STAR facility at ANSTO<sup>42</sup>.

The  $^{14}\text{C}$  ages and related information, including age calibration performed using the SHCal13 calibration curve<sup>43</sup> and the OxCal version 4.2 program<sup>44</sup>, are provided in Supplementary Table 2.

**Single-grain OSL dating.** OSL dating provides a means of determining the burial ages for sediments and associated artefacts and fossils<sup>34–36</sup>. The time that has elapsed since mineral grains were last exposed to sunlight can be determined from measurements of the OSL signal—from which the equivalent dose ( $D_e$ ) is estimated—together with determinations of the radioactivity of the sample and the material surrounding it to a distance of around 30 cm (the environmental dose rate). Fifty-two samples were collected for OSL dating from the upper 2.9 m of deposit during the 2012 and 2015 excavation seasons and from four different excavated profiles (Extended Data Fig. 8). Individual grains of quartz (180–212  $\mu\text{m}$  diameter) were obtained from the samples and measured for their  $D_e$  values, using standard procedures and tests (for example, ref. 45). To obtain an estimate of the environmental dose rate for each sample, an internal alpha dose rate of  $0.032 \pm 0.010 \text{ Gy kyr}^{-1}$  was assumed and beta dose rates were measured using a GM-25-5 beta counter<sup>46</sup> and the procedures described in ref. 47. Gamma dose rates were measured directly by *in situ* gamma spectrometry, and cosmic-ray dose rates were calculated using published equations<sup>48,49</sup>. Beta dose rates were corrected for grain-size attenuation and the beta, gamma and cosmic-ray dose rates were adjusted using a water content of  $5 \pm 2\%$  (68.2% confidence interval) to obtain estimates of the total environmental dose rate. The burial time of the grains in calendar years before present is calculated as the  $D_e$  divided by the environmental dose rate. Age uncertainties are given at the 68.2% confidence level and were estimated by combining, in quadrature, all known and estimated sources of random and systematic error. Details of the preparation, measurement and analysis of single grains, the determination of  $D_e$  values and dose rates, and the resulting OSL age estimates are provided in the Supplementary Information.

Independent estimates of single-grain  $D_e$  values and dose rates were obtained for four samples (SW13A, 11A, 7A and 5A) at the University of Adelaide by L.J.A. In addition, the single-grain  $D_e$  values for four samples reported in the original thermoluminescence dating study of Madjedbebe<sup>13</sup> (KTL158, 162, 164 and 165) were re-measured and their environmental dose rates re-calculated using the same procedures as for the other samples in this study. Details are given in the Supplementary Information and the results are shown in Extended Data Fig. 10.

Single-grain OSL ages were put into a Bayesian statistical model on the OxCal platform (OxCal version 4.2.4)<sup>44,50</sup> (Fig. 3). The samples measured from the NE sample column (Extended Data Fig. 8e) were not included in the model, because there is a slope from the back of the site to the front and the depth offset with the samples collected from the SW and NW sequences is not known with sufficient precision. The model included the two single-grain ages obtained for KTL162 and KTL164 (ref. 16)—re-calculated here using updated dose rate information (Extended Data Fig. 10f)—and the four replicate ages for SW13A, 11A, 7A and 5A obtained independently by L.J.A.

Each OSL age was input as a  $C_{\text{date}}$  in calendar years before AD 1950 with an associated uncertainty (the standard error of the mean). Only the random errors (listed in parentheses in Supplementary Table 5) were included in the model, because OSL ages do not have fully independent uncertainties<sup>51,52</sup>. As prior information, we used the depths associated with changes in artefact technology and stone tool raw materials, and the peaks and dips in artefact concentration (Extended Data Fig. 2). The entire sequence was modelled as a series of seven phases (Fig. 3), assuming that the measured ages are unordered and uniformly distributed within a phase, and the stratigraphically lowest phase is older than those above. A 'boundary' was placed at the start and end of each phase. A General  $t$ -type Outlier Model<sup>53</sup> was used to assess the likelihood of each age being consistent with the fitted model. Each age was assigned a prior outlier probability of 5%. Further details of the Bayesian modelling, together with the modelled OSL data and model code, are provided in the Supplementary Information.

**Archaeobotanical analysis methods.** Sixty litres of sediment for each excavation unit (approximately 100% of a 4 cm spit) was collected from two columns (C3/1–27 and C2/28–57; C6/1–15 and C5/16–72) as a bulk sediment sample, allowing a continuous sequence of archaeobotanical recovery through the deposit. In addition, all hearths and other features were collected in their entirety for flotation. The recovery of archaeobotanical material at Madjedbebe was aided by the use of a cascading 'Ankara-style' flotation tank<sup>54,55</sup>, which facilitated swift and comprehensive processing. Archaeobotanical samples were sorted and weighed. The wood charcoal was separated from the other macrobotanical remains, both examined separately by X.C. and S.A.F. The wood charcoal was taxonomically identified following the criteria of the International Association of Wood Anatomists and with the assistance of a comprehensive wood reference collection for the region collected by X.C. with the assistance of the George Brown Darwin Botanic Gardens<sup>56,57</sup>. Sampling protocols were in accordance with those outlined by Asouti and Austin<sup>58</sup>. The other macrobotanical remains were sorted using standard archaeobotanical procedures. High-powered light microscopy and scanning electron microscope imaging was used to compare the anatomical and morphological features of the archaeological specimens to modern reference material from the region (collected



by S.A.F. in conjunction with the Gundjeihmi Aboriginal Corporation, Mirarr traditional owners and the Northern Territory Herbarium). We used the criteria proposed by Fairbairn<sup>59</sup> and Hather<sup>60,61</sup> to identify *Pandanus* sp. drupes and vegetative parenchyma, respectively.

**Artefact associations and refitting.** Refitting attempts were made on all plotted and 7-mm-sieve silcrete artefacts as well as all 3-mm-sieve silcrete artefacts from squares C2–C4 ( $n = 778$ ). A traditional approach to refitting was combined with high resolution, objective measurements of artefact colour to determine potential matches between similarly coloured artefacts. This method used a portable, wireless colour scanner (NODE+ Chroma 2.1 by Variable Inc.) that communicates with handheld iOS and Android devices. An application program interface for each device was produced to allow the collection of identification-tied data, and a project-specific.net application that allowed transparent statistical analysis and colour grouping of data was also produced<sup>62</sup>. Refits were first attempted between all artefacts grouped by similar colour, and then across colour grades. Scans were restricted to a section of the lithic artefact where NODE+ either sits flush with the surface or on a slight concavity that rises to meet the aperture. This maintained a standard measurement distance during each scan. A minimum of three suitable scanning areas was identified on each artefact, with five scans taken from each sample area. Five scans were taken to minimize the potential of any human error during positioning of the device. For banded or variably coloured artefacts, each area of colour was treated as a separate sample area. Potential matching artefacts were analysed for similarity under 10× and 20× magnification using an Olympus SZX16 stereoscope with NIS Elements Advanced Research version 4, following the methodology outlined by Wilkins<sup>63</sup>.

**Granulometry.** Hand-grab bulk samples were taken from squares B2, C4, and E2 at 5 cm intervals from the surface, dry sieved through a 2-mm screen and macroscopic organic materials were removed by hand. For each sample, three trials of five sub-samples were analysed with a Horiba LA-950 Laser Particle Size Analyser at the University of Washington, Department of Materials Science and Engineering, resulting in 15 measurements per sample.

**Carbon isotopes.** Hand-grab bulk samples were collected from square B2, following the procedure for granulometry. A 2 g sub-sample was then ground to a fine powder and treated with 2 M HCl for 24 h to remove inorganic carbon. The samples were then rinsed in de-ionized water, the water separated from the sediments using a centrifuge, and the samples dried at 60 °C for 24 h and then measured using a Costech Elemental Analyser on a Finnigan 253 Mass Spectrometer at the IsoLab in the University of Washington, Department of Earth and Space Sciences.

**Micromorphology.** Intact blocks of sediment were extracted from squares B2 and E2, and the hearth at C4/36A, by encasing the blocks in plaster bandages to ensure their integrity. The blocks were air-dried at 40 °C for seven days, then impregnated with Reichhold PolyLite polyester resin, styrene and hardened with methyl ethyl ketone peroxide using a ratio of 7:3:0.025. After curing for several weeks, thick sections were cut from the blocks with a diamond saw and sent to Spectrum Petrographics to prepare thin sections for microscopic analysis. Thin sections were analysed under different magnifications and different lights (plane polarized, cross-polarized and fluorescent) with stereo petrographic microscopes at the University of Tübingen and the University of Washington. Whole-slide scans were taken with a flat-bed document scanner.

**Magnetic susceptibility.** Magnetic susceptibility ( $\chi$ ) was measured at both low (460 Hz) and high (4,600 Hz) frequencies for the stratigraphic units within the sedimentary sequence in squares B2 and C3. As observed in other sandstone rock shelters<sup>64,65</sup>, samples are weakly magnetic in the culturally sterile layers. The lower susceptibility values measured in the deepest deposits were often close to the sensitivity limit of the Bartington Instrument MS2B sensor, resulting in a higher percentage loss of the low-frequency measurements ( $\chi_{fd}\%$ ), with averages of around 16%; these data were discarded.

**Pigment characterization.** *X-ray fluorescence.* Non-invasive elemental characterizations were undertaken to investigate the inorganic chemical composition of pigments. Data were collected using a Bruker S1 Titan 800 portable X-ray fluorescence (pXRF) instrument, equipped with a silicon drift detector, Rh target X-ray tube (maximum voltage 50 kV, default to 150 °C with ultralene window) and five-position motorized filter changer. Two beam phases were run sequentially, each collecting for 90 analytic seconds. Phase 1 parameters: 45 kV, 10.45  $\mu$ A with a filter (Ti 25  $\mu$ m, Al 300  $\mu$ m) in the beam path. Phase 2 parameters: 15 kV, 31.55  $\mu$ A without a filter. Spectra were collected on suitable artefact surfaces, where attenuation could be minimized or avoided<sup>66</sup>. Relative abundance concentrations for 27 elements reported derive from the manufacturer's fundamental parameters calculation.

*Synchrotron powder diffraction.* Powder pigments were collected using a micro-drill, two from ART9 with an additional 75 samples taken from ochre nodules by milling the outside of the specimens and then drilling to a depth of around 5 mm

to sample their internal structure. Powders were homogenized (manually ground with mortar and pestle), placed into 0.3-mm-diameter borosilicate capillaries and mounted on the beamline. Diffraction data were collected at the Australian Synchrotron at a wavelength of 0.77412 Å, calibrated using a NIST SRM 660b, from 5–85° 2Theta, with a Mythen microstrip detector with an inherent step size of 0.002°, using two detector positions and a collection time of 5 min per position. Samples were rotated at around 1 Hz during data collection to ensure good powder averaging. Phase identifications of selected samples were undertaken using Panalytical Highscore with the ICDD PDF4 database.

**Usewear and residues.** All potential grinding stones and fragments ( $n = 91$ ) from the 2012 excavations were examined for wear and residue traces. Stones were visually scanned under low and high magnification on the ground and unground surfaces, using stereo and metallographic microscopes with low-angled oblique light and vertical incident light sources, respectively. The unground surfaces were documented to evaluate residues and traces that might be linked to handling or anvil positioning during use, and to identify traces that mimic usewear, such as micro-fractures of quartz grains on non-used surfaces. The latter are probably caused by friction between sediment and artefacts, either during use or after discard and burial within the sediments. All complete, near-complete and broken edge-ground hatchets ( $n = 10$ ), and a selection of flakes from edge-ground axe margins, were also examined under the same stereo and metallographic microscopes.

Residue distributions were documented across each of the tool surfaces and characterized using a range of techniques, following removal with a solvent mixture of water, ethanol and acetonitrile (up to 50  $\mu$ l extracted with an adjustable pipette). Residue extractions were characterized using: (1) high-magnification transmitted light microscopy and various biochemical stains to test for and distinguish plant and animal tissues; (2) absorbance spectroscopy and biochemical tests for the detection of protein, carbohydrates, fatty acids, starch and ferrous iron (see ref. 67 and Supplementary Information for specific methods for each test); and (3) gas chromatography mass spectrometry. A selection of grinding stones ( $n = 12$ ) had additional residues removed by ultrasonication. Tools were completely or partially submerged in distilled water and ultrasonicated for 2 min. Density separation of the extracted residue mixtures isolated starch grains and other plant microfossils (phytoliths, raphides, pollen), when present.

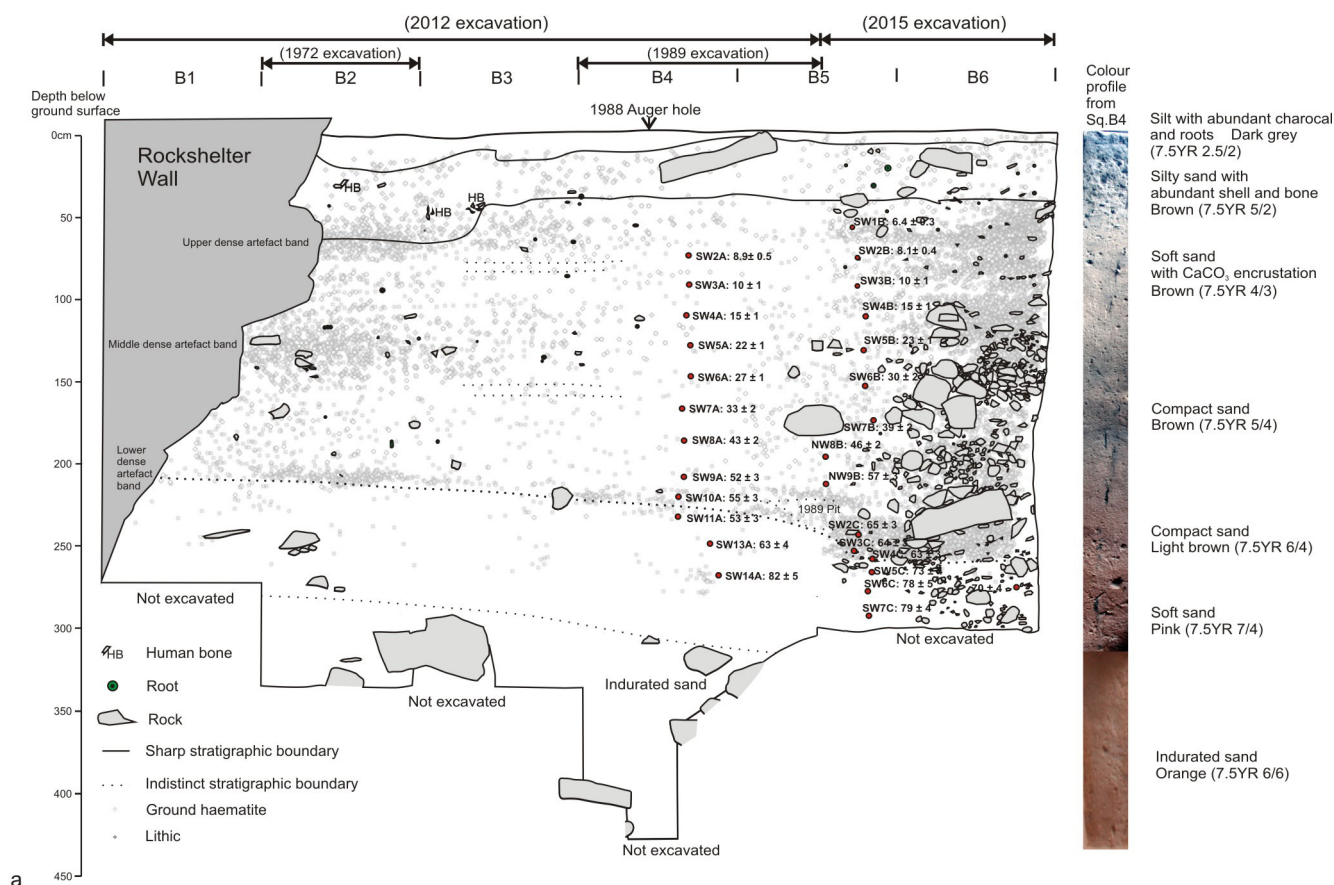
**Code availability.** The computer code used to generate the Bayesian age model for the site is provided in full in the Supplementary Information, together with information about the program and version used. The R code used to analyse and visualize the geoarchaeological and stone artefact data is archived online at <https://doi.org/10.6084/m9.figshare.4652536>.

**Data availability.** All elements necessary to allow interpretation and replication of results, including full datasets and detailed experimental procedures are provided in the Supplementary Information. All geoarchaeological and stone artefact data files are archived online at <https://doi.org/10.6084/m9.figshare.4652536>. Archaeological material generated in this study will be kept in the Archaeology Laboratories of the University of Queensland until 2018. It will then be deposited in a Gundjeihmi Aboriginal Corporation keeping place. The material will be publicly accessible upon request with permission from Gundjeihmi Aboriginal Corporation and the corresponding author. Archaeological materials from the 1973 and 1989 excavations are stored in the Museum and Art Gallery of the Northern Territory and can be publicly accessed with permission from the museum director.

- Hua, Q. *et al.* Progress in radiocarbon target preparation at the Antares AMS Centre. *Radiocarbon* **43**, 275–282 (2001).
- Fink, D. *et al.* The ANTARES AMS facility at ANSTO. *Nucl. Instrum. Methods Phys. Res. B* **223–224**, 109–115 (2004).
- Hogg, A. G. *et al.* SHCal13 Southern Hemisphere calibration, 0–50,000 years cal BP. *Radiocarbon* **55**, 1889–1903 (2013).
- Bronk Ramsey, C. & Lee, S. Recent and planned developments of the program OxCal. *Radiocarbon* **55**, 720–730 (2013).
- Wood, R. *et al.* Towards an accurate and precise chronology for the colonization of Australia: the example of Riwil, Kimberley, Western Australia. *PLoS ONE* **11**, e0160123 (2016).
- Bøtter-Jensen, L. & Mejdahl, V. Assessment of beta dose-rate using a GM multicounter system. *Int. J. Rad. Appl. Instrum. D* **14**, 187–191 (1988).
- Jacobs, Z. & Roberts, R. G. An improved single grain OSL chronology for the sedimentary deposits from Diepkloof Rockshelter, Western Cape, South Africa. *J. Archaeol. Sci.* **63**, 175–192 (2015).
- Prescott, J. R. & Hutton, J. T. Cosmic ray contributions to dose rates for luminescence and ESR dating: large depths and long-term time variations. *Radiat. Meas.* **23**, 497–500 (1994).
- Smith, M. A., Prescott, J. R. & Head, M. J. Comparison of <sup>14</sup>C and luminescence chronologies at Puritjarra rock shelter, central Australia. *Quat. Sci. Rev.* **16**, 299–320 (1997).
- Bronk Ramsey, C. Bayesian analysis of radiocarbon dates. *Radiocarbon* **51**, 337–360 (2009).

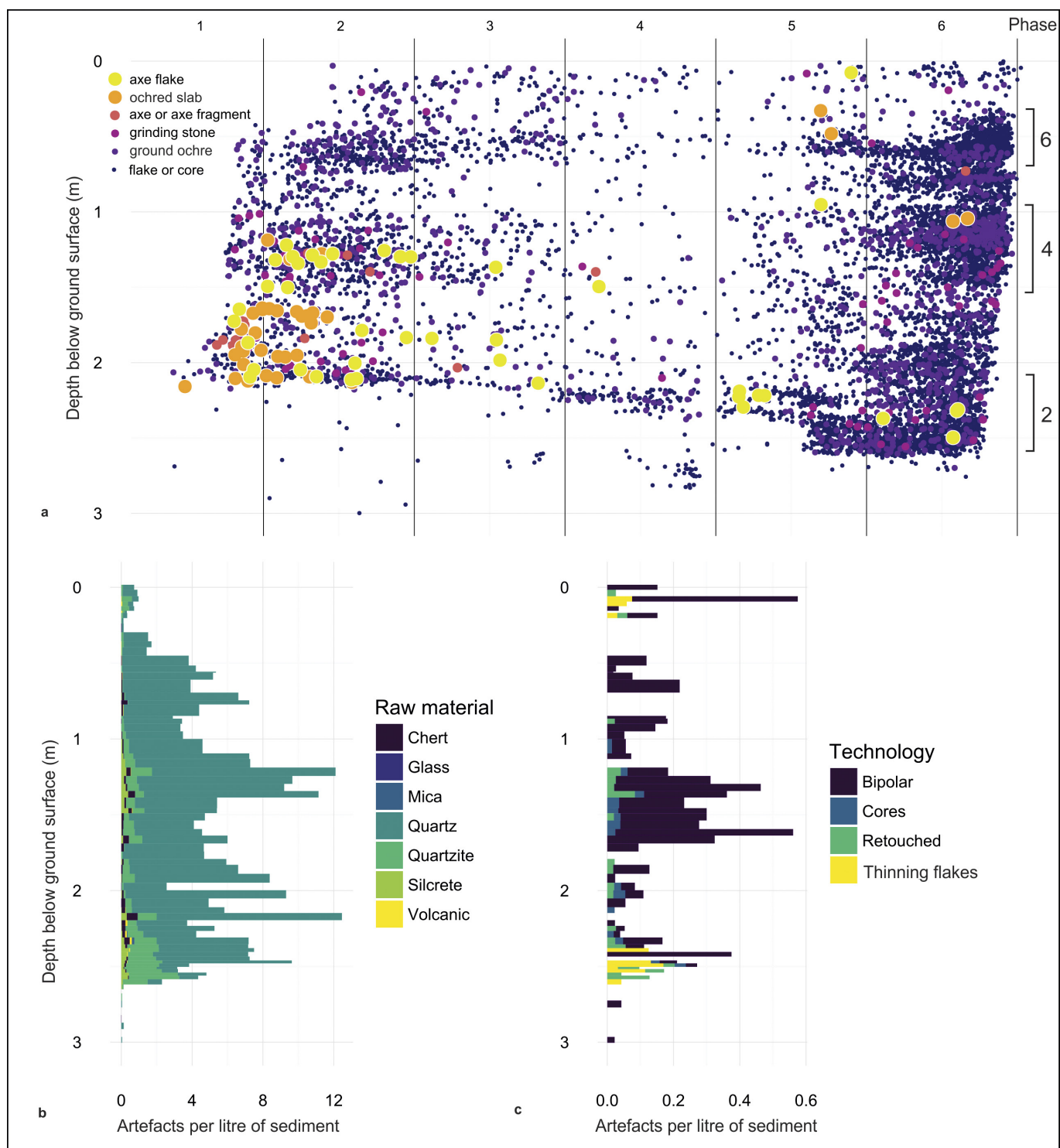
51. Rhodes, E. J. *et al.* Bayesian methods applied to the interpretation of multiple OSL dates: high precision sediment ages from Old Scatness Broch excavations, Shetland Isles. *Quat. Sci. Rev.* **22**, 1231–1244 (2003).
52. Galbraith, R. F. & Roberts, R. G. Statistical aspects of equivalent dose and error calculation and display in OSL dating: an overview and some recommendations. *Quat. Geochronol.* **11**, 1–27 (2012).
53. Bronk Ramsey, C. Dealing with outliers and offsets in radiocarbon dating. *Radiocarbon* **51**, 1023–1045 (2009).
54. French, D. H. An experiment in water-sieving. *Anatol. Stud.* **21**, 59–64 (1971).
55. Nesbitt, M. Plants and people in Ancient Anatolia. *Biblic. Archaeol.* **58**, 68–81 (1995).
56. Wheeler, E. A., Baas, P. & Gasson, P. E. IAWA list of microscopic features for hardwood identification. *IAWA Bull.* **10**, 219–332 (1989).
57. Richter, H. G., Grosser, D., Heinz, I. & Gasson, P. E. IAWA list of microscopic features for softwood identification. *IAWA J.* **25**, 1–70 (2004).
58. Asouti, E. & Austin, P. Reconstructing woodland vegetation and its exploitation by past societies, based on the analysis and interpretation of archaeological wood charcoal macro-remains. *Environ. Archaeol.* **10**, 1–18 (2005).
59. Summerhayes, G. R. *et al.* Human adaptation and plant use in highland New Guinea 49,000 to 44,000 years ago. *Science* **330**, 78–81 (2010).
60. Hather, J. G. in *Tropical Archaeobotany: Applications and New Developments* (ed. Hather, J. G.) 51–64 (Routledge, 1994).
61. Hather, J. G. *Archaeological Parenchyma* (Archetype Publications, 2000).
62. McNeil, J.-L., Marginson, A., Mackay, A. & Clarkson, C. Colour Signature Analysis: Using objective colour quantification techniques towards refitting lithic assemblages. 80th Annual Meeting of the Society for American Archaeology (2015).
63. Wilkins, J. R. *Prepared Core Technology at Kudu Koppie, South Africa and the Modern Human Behaviour Debate*. MA thesis, Univ. Calgary (2008).
64. Lowe, K. M. *et al.* Using soil magnetic properties to determine the onset of Pleistocene human settlement at Gledswood Shelter 1, northern Australia. *Geoarchaeology* **31**, 211–228 (2016).
65. Lowe, K. M., Mentzer, S. M., Wallis, L. A. & Shulmeister, J. A multi-proxy study of anthropogenic sedimentation and human occupation of Gledswood Shelter 1: exploring an interior sandstone rockshelter in Northern Australia. *Archaeol. Anthropol. Sci.* <http://dx.doi.org/10.1007/s12520-016-0354-8> (2016).
66. Huntley, J. Taphonomy or paint recipe? *In situ* portable X-ray fluorescence analysis of two anthropomorphic motifs from the Woronora plateau, New South Wales. *Aust. Archaeol.* **75**, 78–94 (2012).
67. Fullagar, R. *et al.* Evidence for Pleistocene seed grinding at Lake Mungo, south-eastern Australia. *Archaeol. Oceania* **50**, 3–19 (2015).





**Extended Data Figure 1 | Madjedbebe rock shelter.** a, Section drawing of the southwest profile wall, showing major stratigraphic divisions and sediment descriptions, and the location of the 1973, 1989, 2012 and 2015

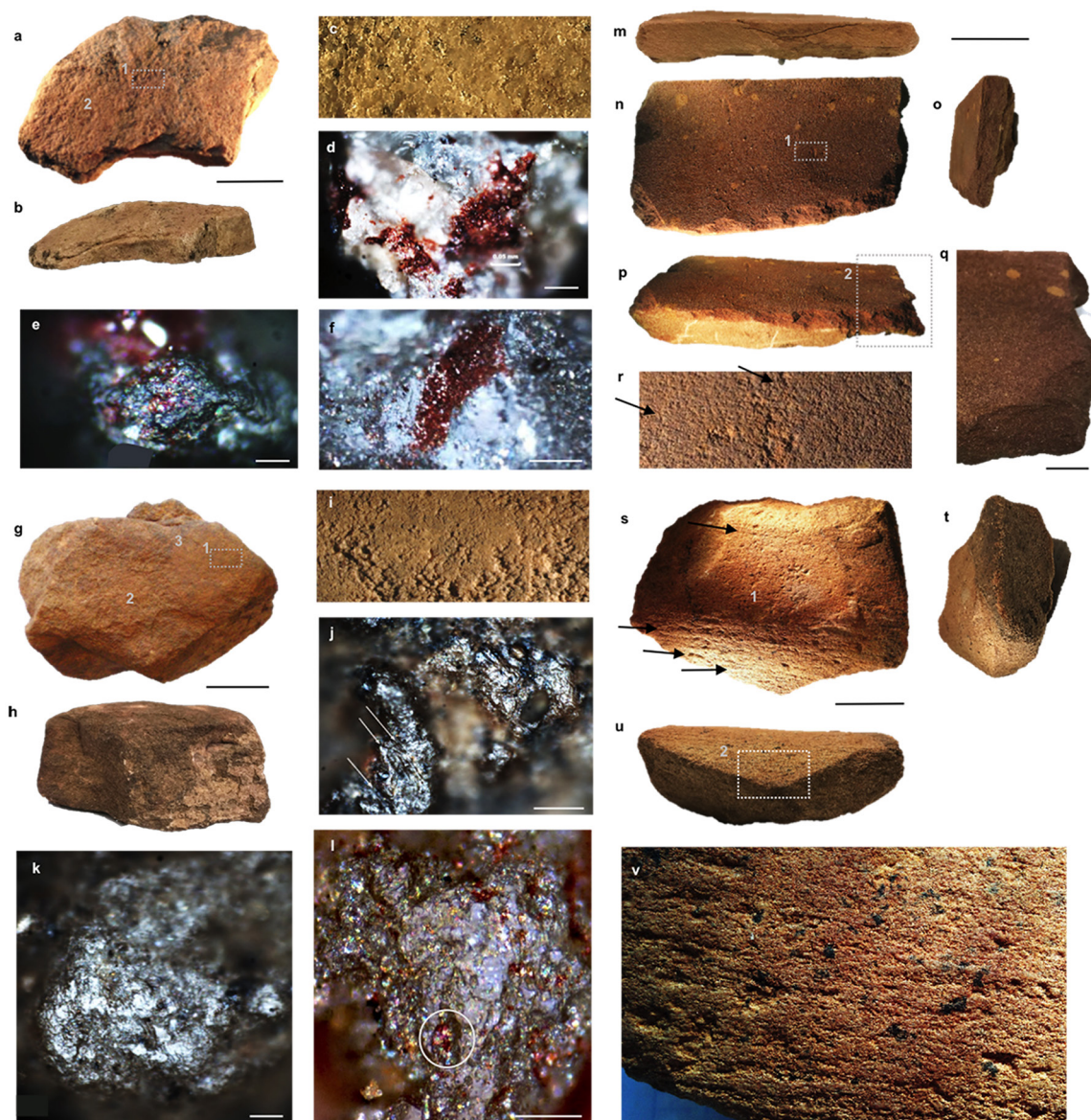
excavation trenches. Light grey dots show plotted artefacts. b, Photograph of the site during the 2015 excavation. c, Detail of the site ground surface during ground penetrating radar survey, before the 2012 excavation.



**Extended Data Figure 2 | Plot of artefact densities and assemblage composition as a function of depth below ground surface.** **a**, Plot of density of artefacts found during the 2012 and 2015 excavation seasons in squares from the C and B rows. Artefacts are shown by type (axe flake, ochred slab, axe or axe fragment, grinding stone, ground ochre, and flake or core) superimposed on the southwest profile wall (Extended Data Fig. 1).

Phases represent the three dense artefact bands (see text and Supplementary Information). **b**, Plot of artefact density and raw material type with depth, based on plotted artefacts and residue found in the 7-mm sieves for square B6. **c**, Plot of technological changes with depth, based on plotted artefacts and residue found in the 7-mm sieves for square B6.

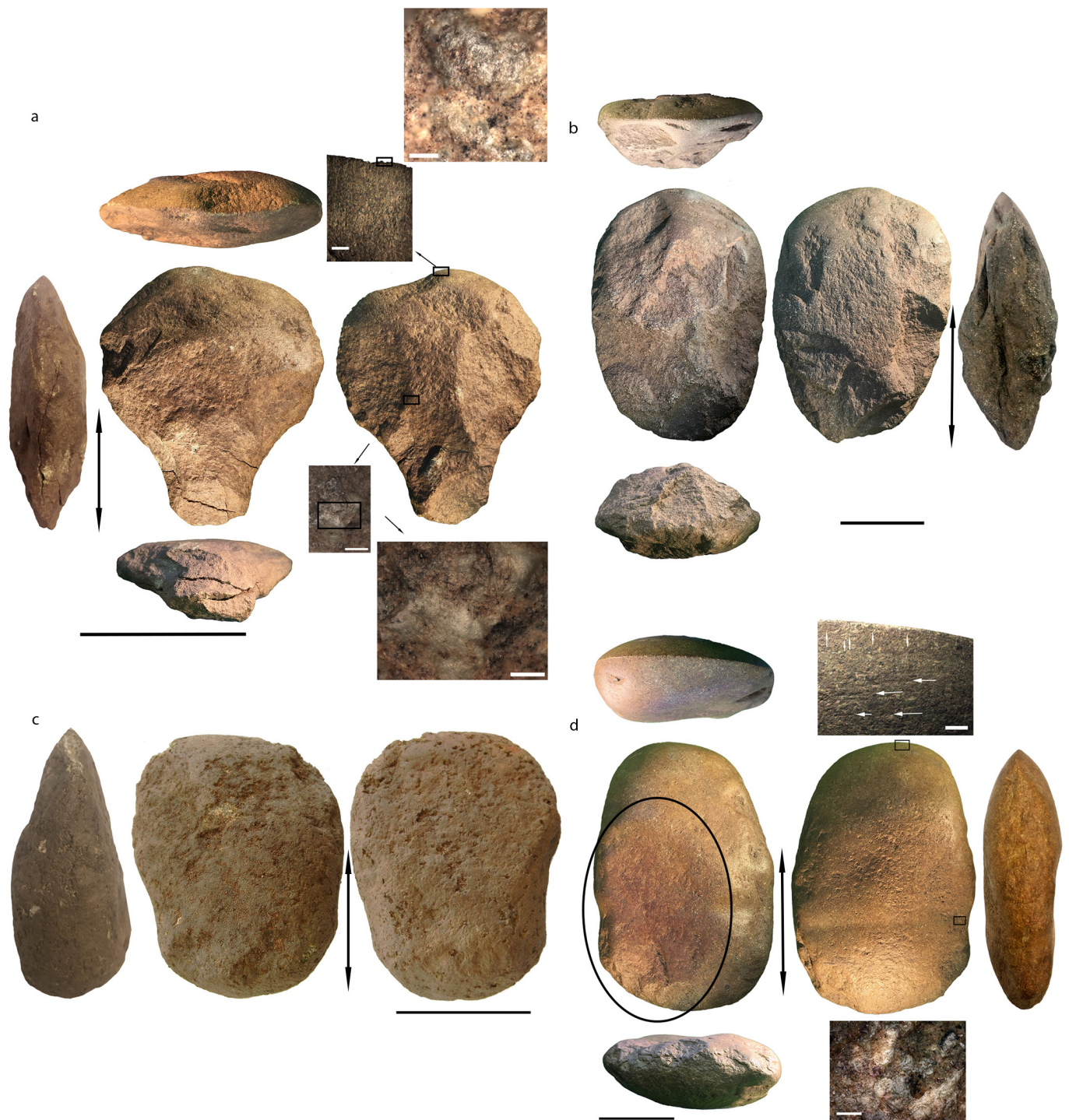




**Extended Data Figure 3 | Grinding stones, residues and usewear of specimens collected from phase 2 at Madjedbebe.** **a–f**, Specimen UPGS36 (from 2012 spit 44) and residues from processing of red pigment. **a**, Ground surface. Scale bar, 2 cm. **b**, Plan view. **c**, Ground surface at low magnification (location 1 in **a**) showing levelled grains. **d–f**, Red pigment residues at high magnification. **d**, Location 2 in **a**. Scale bar, 0.5 mm. **e**, **f**, Location 2 in **a**. Scale bars, 0.02 mm. **g–k**, Specimen GS39 (from 2012 spit 37) and usewear, used for processing of seeds. **g**, Ground surface. Scale bar, 4 cm. **h**, Plan view. **i**, Ground surface at low magnification (location 1 in **g**) showing levelled and rounded grains. **j**, Bright use-polish with striations (arrows, location 2 in **g**). Scale bar, 0.1 mm. **k**, Bright, reticulated use-polish (location 3 in **g**). Scale bar, 0.05 mm. **l**, Specimen GS73 (from

2015 spit 52): bright, undulating use-polish, with red pigment residues in the lowest regions of the grains (circle, location 1 in **s**). Scale bar, 0.05 mm. **m–r**, Specimen GS79 (from 2015 spit 54) used for the manufacture and sharpening of stone hatchets. **m**, Plan view. Scale bar, 5 cm. **n**, Ground surface. **o**, Side view. **p**, Angled view, upper surface is ground, note the flake margins. **q**, Location 2 in **p** showing flake scars. **r**, Ground surface at low magnification (location 1 in **n**) showing levelled grains and deep striations (arrows). **s–v**, Fragment of GS73 with deep partial grooves: **s**, Ground surface. Scale bar, 5 cm. **t**, Side view. **u**, Plan view. **v**, Ground surface at low magnification, note the deep striations and red surface staining (location 2 in **u**).

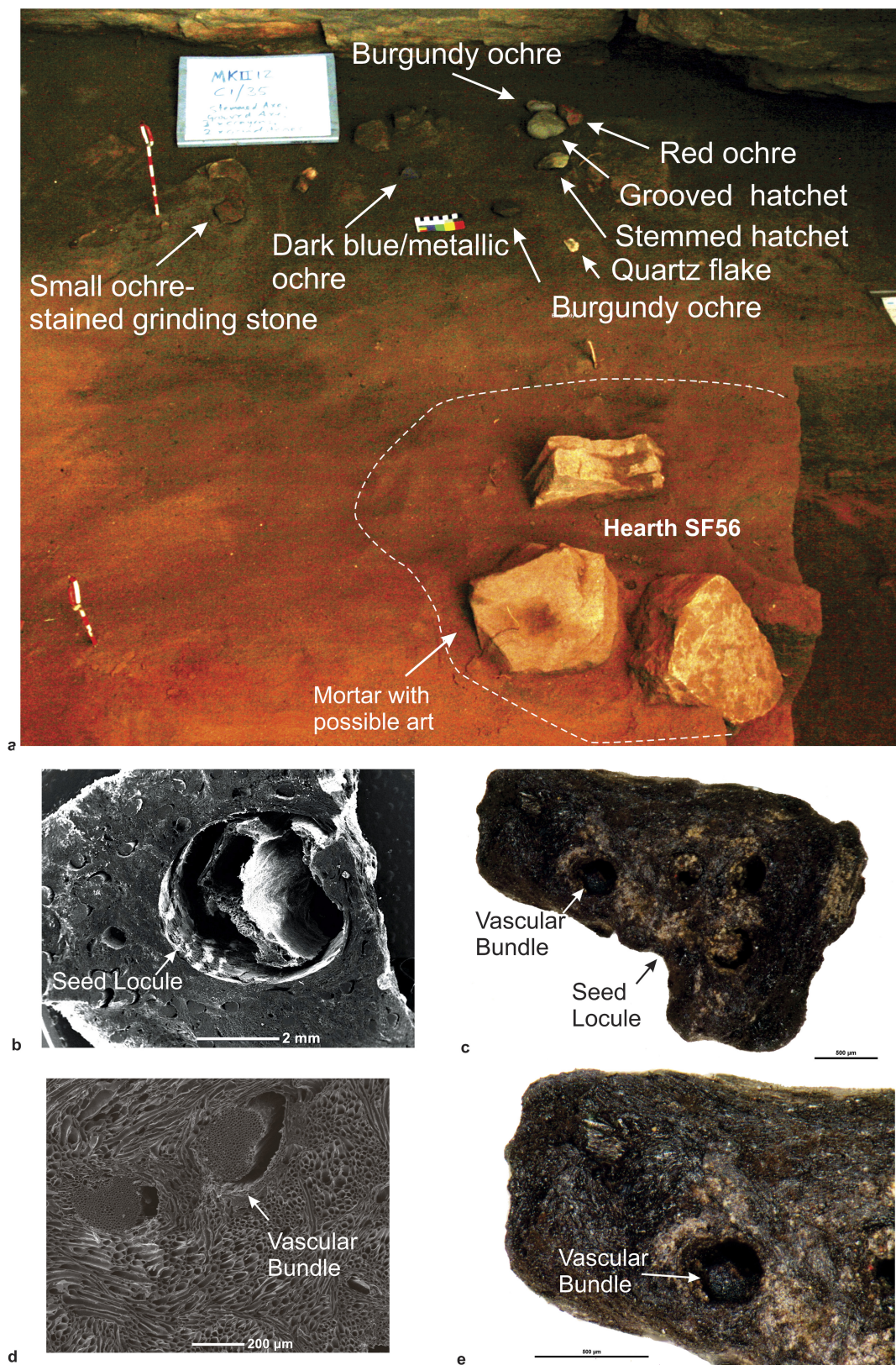




**Extended Data Figure 4 | Dolerite edge-ground hatchet heads showing plan and end views.** Main scale bars are 5 cm. Vertical double-ended arrows indicate the haft zones. **a**, EGH7 from unit C1/35 (base of phase 3) with shouldered or stemmed design for a haft. Two upper insets show (left; scale bar, 2 mm) striations from grinding and (right; scale bar, 0.2 mm) polish from use. The lower insets show (left; scale bar, 0.2 mm) wear from haft movement and (right; scale bar, 0.01 mm) detail of the polish (smooth white zones) and possible resin (red smears with black

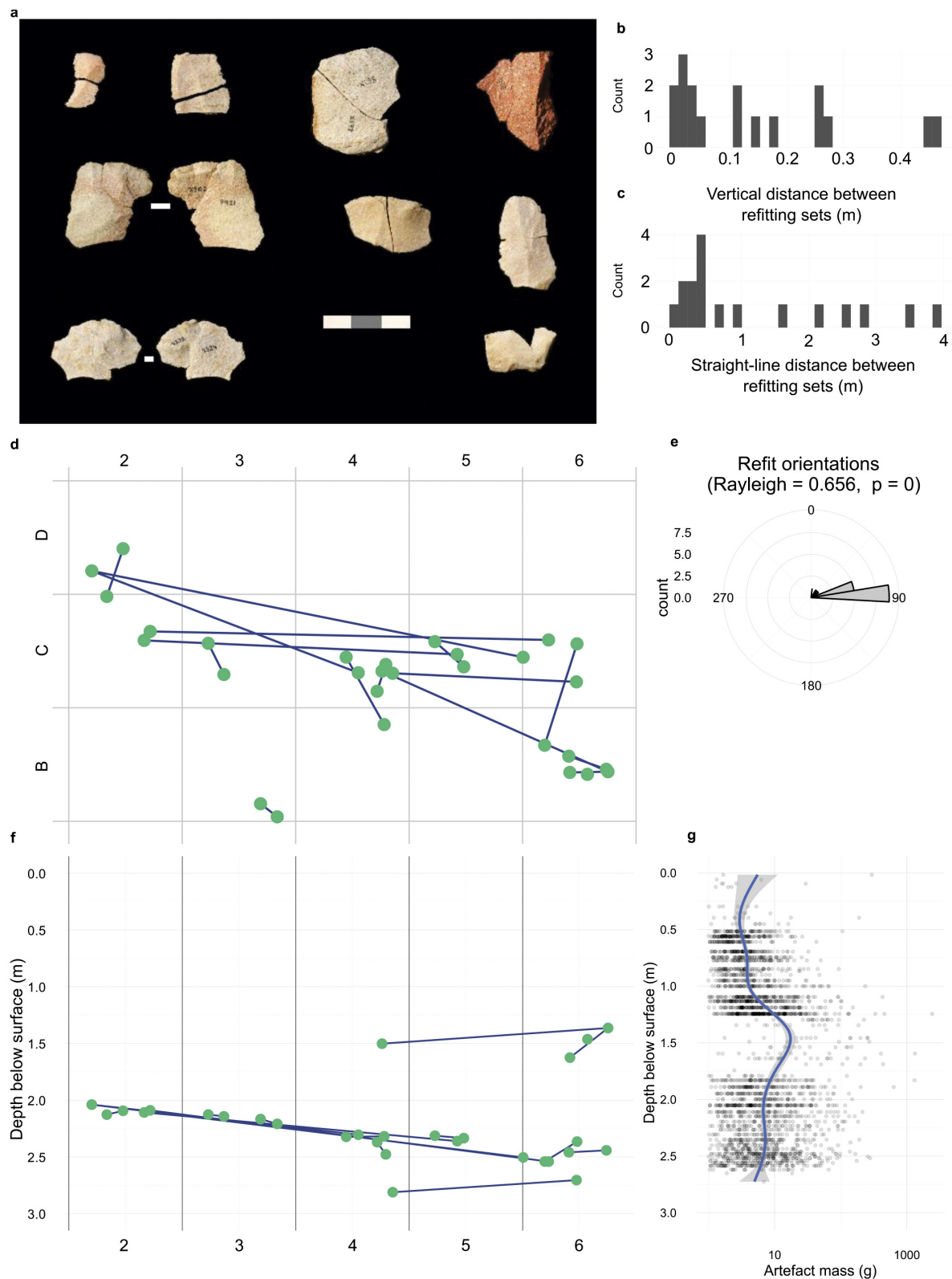
spots). **b**, EGH1 from unit C1/33 (phase 4) with large flake scarring and cracks within the haft zone. **c**, EGH8 from unit C1/38 (base of phase 3) with a slight waist design for a haft. **d**, EGH6 from C1/33 (phase 3) with grooved design for a haft and red stain from mixing pigment (ellipse). The upper inset (scale bar, 2 mm) shows traces of use (vertical arrows) and grinding (horizontal arrows). The lower inset (scale bar, 0.2 mm), from inside the groove, shows polish from haft movement.





**Extended Data Figure 5 |** Hearth SF56 with grindstones and carbonized *Pandanus* drupe from a hearth in spit C2/41. **a**, Photograph of hearth pit SF56 in C4/35 (phase 3) showing *in situ* grinding stones in a hearth with elevated magnetic susceptibility readings, and a probable cache of ground ochre, grindstones and hatchet heads against the back wall.

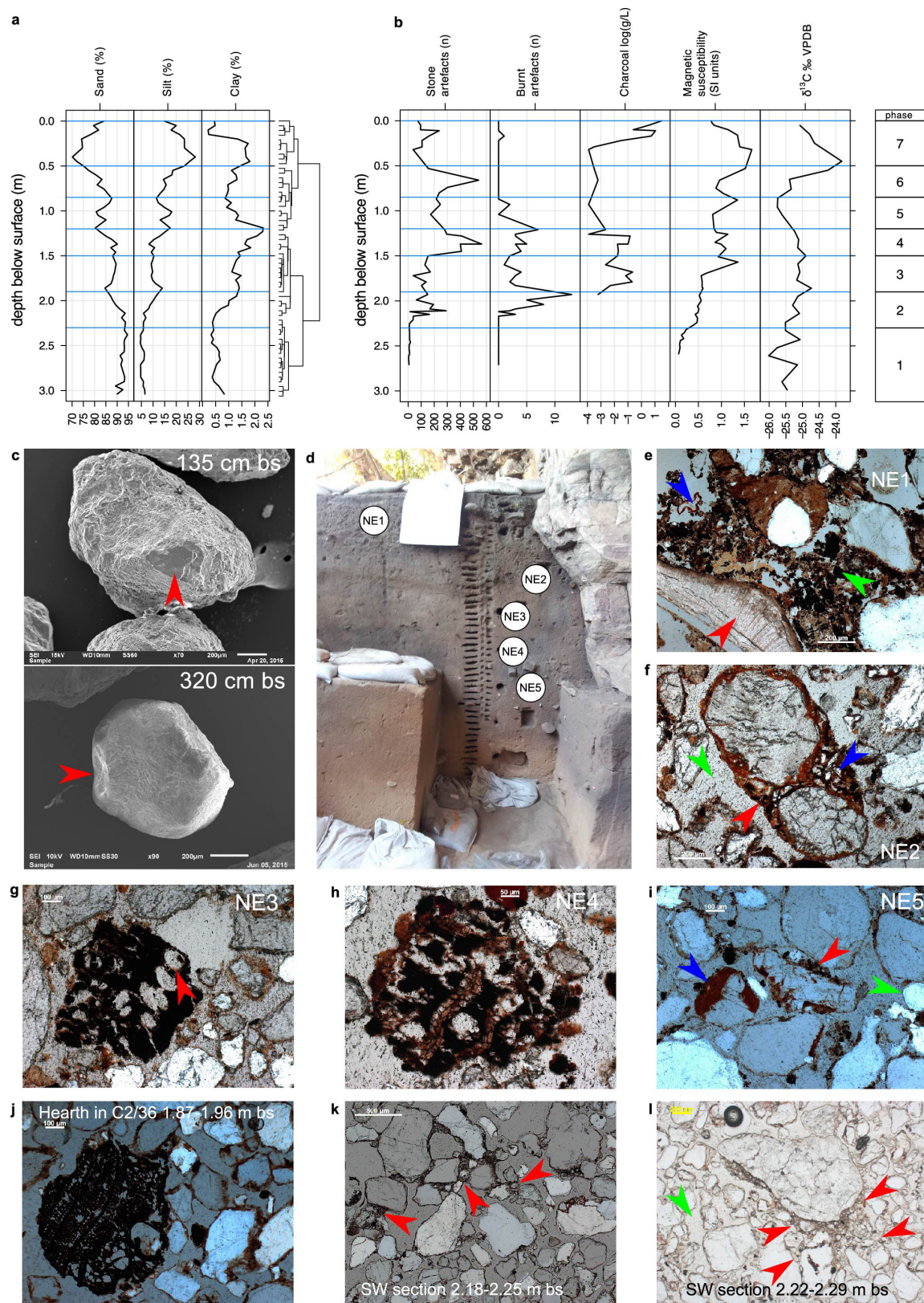
**b, d**, Scanning electron microscope images of modern reference specimen 2639, *Pandanus spiralis* drupe (13× and 90× magnifications, respectively). **c, e**, Photographs of archaeological specimen C2/41(1), *Pandanus* sp. drupe. Note the seed locule, vascular bundles and flaring ground tissue apparent on both modern reference and archaeological specimens.



**Extended Data Figure 6 | Summary of Madjedbebe silcrete artefact refitting analysis.** **a**, Selection of refitting and conjoining artefacts; scale bar intervals, 10 mm. **b**, Histogram showing the distribution of vertical distances between refitting artefact fragments. The median vertical refit distance is 0.10 m, with a median absolute deviation of 0.13 m. **c**, Histogram showing the distribution of straight-line distances between refitted artefact fragments. The median straight-line refit distance is 0.44 m, with a median absolute deviation of 0.47 m. **d**, Plan view showing the refitted artefacts at the locations where they were found at the time of excavation. Blue lines connect refitted pieces. Annotations on the

axes show the excavation grid coordinates. **e**, Polar plot of horizontal orientations of the vector between pairs of refitted pieces. The Rayleigh test result indicates a significantly non-random distribution. For most refits, both artefacts in the refit pair were recovered from the same horizontal plane. **f**, Section view showing the refitted artefacts at the locations where they were found at the time of excavation. Blue lines connect refitted pieces. **g**, Plot of artefact mass by depth in square B6: each point represents one artefact, the blue line is a robust locally weighted regression, and the grey band is the 95% confidence region for the LOWESS regression line.



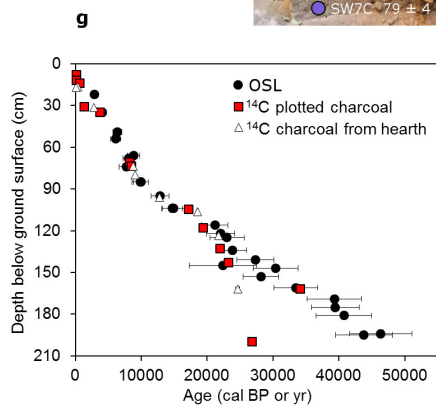


Extended Data Figure 7 | See next page for caption.



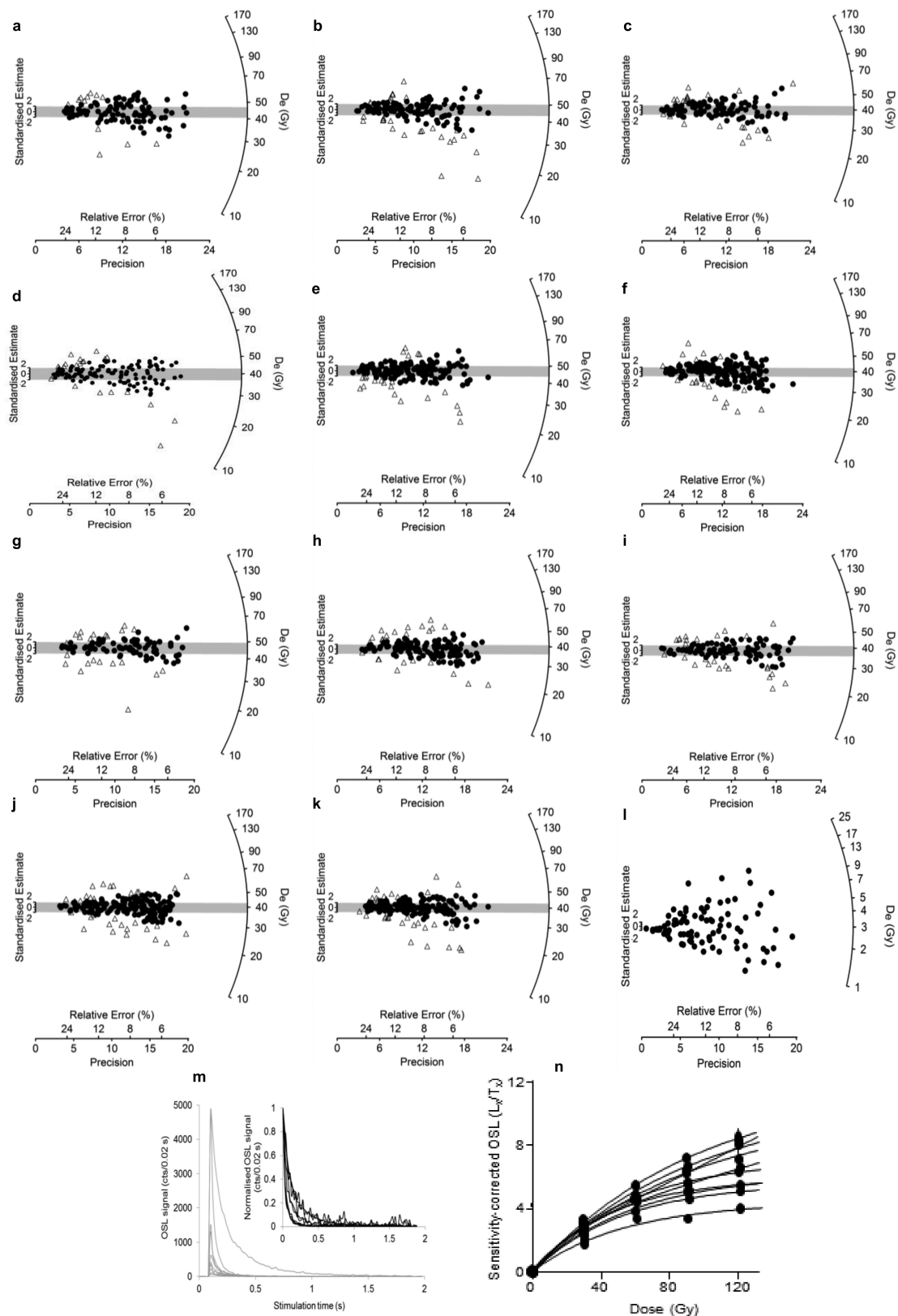
**Extended Data Figure 7 | Summary of Madjedbebe geoarchaeological analysis.** **a**, Particle size distributions of bulk samples extracted from the southwest wall of square D3 (left) and constrained cluster analysis dendrogram (right). Blue horizontal lines indicate the artefact discard phases, calibrated for squares C3 and D3. **b**, Distributions of key geoarchaeological variables measured on bulk samples extracted from the southwest wall of square D3. Magnetic susceptibility units are  $10^{-7} \text{ m}^3 \text{ kg}^{-1}$ ; VPDB is Vienna Pee Dee Belemnite, an international reference standard for  $\delta^{13}\text{C}$  analysis. **c**, Scanning electron microscope images of sand grains from 1.35 m (top) and 3.20 m (bottom) depth below surface (bs). **d**, Photograph of the northeast section of the 2012 excavation area. Labels in white circles indicate locations of micromorphology samples. **e**, Micromorphology sample NE1 from the midden deposit showing shell fragment (red arrow), charcoal (green arrow) and root fragment (blue arrow). **f**, Micromorphology sample NE2 from the lower

midden deposits showing linked-capped grains (red arrow), silt (blue arrow) and voids (green arrow). **g**, Micromorphology sample NE3 from below the midden showing weathered charcoal fragment with clay infill (red arrow). **h**, Micromorphology sample NE4 showing an extensively weathered charcoal fragment. **i**, Micromorphology sample NE5 showing grain with silty coating (red arrow), grain with clay coating (blue arrow) and grain with no coating (green arrow). **j**, Micromorphology sample from the C2/36 hearth feature showing a well-preserved charcoal fragment. **k**, Micromorphology sample from the southwest section of square D3 (2.18–2.25 m depth below surface) showing linked-capped grains (red arrows), similar to sample NE2. **l**, Micromorphology sample from the southwest section of square D3 (2.22–2.29 m depth below surface) showing packing voids (green arrow) and a polymineral grain with linked-capping joining it with smaller grains (red arrows).



**a**, Two-dimensional site plan of excavated squares, showing the locations of the OSL sample series. Grey-shaded squares represent squares from which charcoal samples were collected for  $^{14}\text{C}$  dating. **b**, Three-dimensional site plan, showing both horizontal and vertical positions of the OSL sample series. Samples shown in the same colour were taken from section walls with the same orientation. **c–f**, Photographs of the

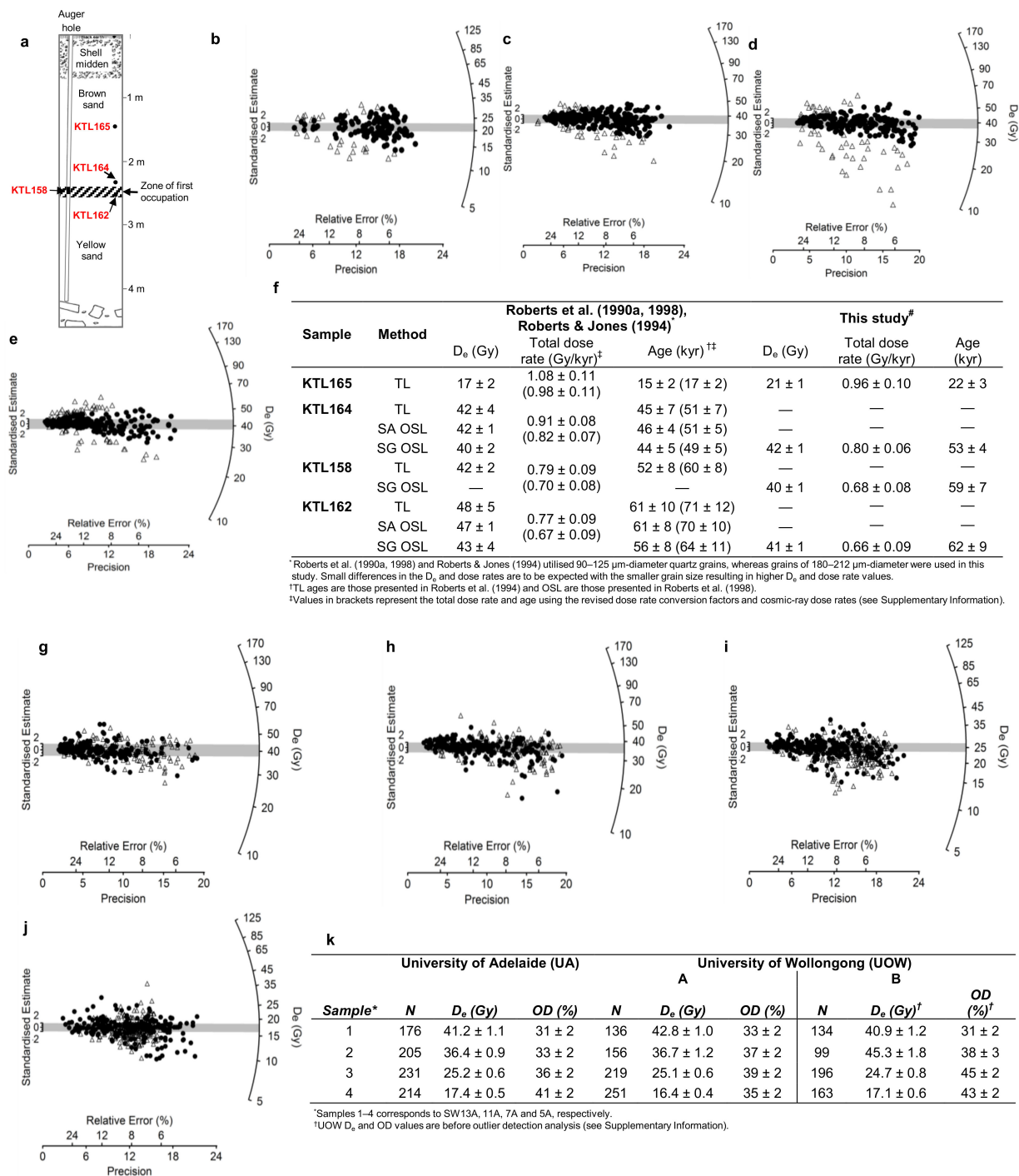
sedimentary deposit for each of the walls from which OSL samples were collected, together with the OSL ages (uncertainties at 68.2% confidence level) and the lowest dense artefact band (phase 2) demarcated by the stippled lines. **c**, Southwest wall of square B5. **d**, Southwest wall of square B6. **e**, Northeast wall of square E2. **f**, Northwest wall of square C4. **g**, Comparison of  $^{14}\text{C}$  and OSL ages (uncertainties at 95.4% confidence level) obtained in this study from the upper 2 m of deposit.



**Extended Data Figure 9 | OSL data for individual sand-sized grains of quartz.** **a–k**, Radial plots of single-grain  $D_e$  values for each sample within the lowest dense artefact band (phase 2). **a**, SW4C; **b**, SW3C; **c**, NW14; **d**, SW13A; **e**, SW2C; **f**, NW13; **g**, SW11A; **h**, NW12; **i**, NW11; **j**, SW10A; **k**, NW9B. **l**, Radial plot of  $D_e$  values for single grains of sample NE1, collected from the shell midden at the top of the sequence. The grey bands in each plot are centred on the weighted mean  $D_e$

determined for each dose population using the central age model, after the rejection of outliers (shown as open triangles). **m**, OSL decay curves for a representative sample of grains from SW13A that span the range of observed luminescence sensitivities (that is, their relative brightness). The inset plot shows the same curves on a normalized  $y$  axis. **n**, Corresponding dose response curves for the grains shown in **m**.





Sample	Water (%)	Radionuclide specific activities (Bq/kg)						Environmental dose rate (Gy/kyr)				Age (kyr)	
		<sup>238</sup> U	<sup>226</sup> Ra	<sup>210</sup> Pb	<sup>228</sup> Ra	<sup>228</sup> Th	<sup>40</sup> K	UA		UOW		UA	UOW
								Beta	Beta	Gamma	Gamma		
1	5 ± 2	8.9 ± 1.7	9.2 ± 0.3	9.0 ± 1.8	16.1 ± 0.8	16.7 ± 0.6	26.1 ± 2.9	0.22 ± 0.02	0.25 ± 0.02	0.28 ± 0.02	0.30 ± 0.01	69.3 ± 5.1	67.3 ± 3.5
2	5 ± 2	12.0 ± 1.5	11.0 ± 0.4	12.8 ± 2.1	19.1 ± 0.9	19.5 ± 0.6	36.3 ± 3.1	0.29 ± 0.02	0.28 ± 0.02	0.35 ± 0.02	0.35 ± 0.02	49.5 ± 3.3	50.2 ± 2.9
3	5 ± 2	12.2 ± 1.8	12.5 ± 0.4	13.0 ± 1.9	21.3 ± 0.8	21.9 ± 0.6	38.3 ± 3.0	0.31 ± 0.02	0.32 ± 0.02	0.38 ± 0.02	0.33 ± 0.02	32.0 ± 2.0	33.4 ± 1.7
4	5 ± 2	13.0 ± 1.5	12.3 ± 0.3	13.6 ± 2.3	19.6 ± 0.8	20.2 ± 0.6	35.1 ± 2.9	0.30 ± 0.02	0.31 ± 0.02	0.36 ± 0.02	0.38 ± 0.02	22.7 ± 1.6	21.0 ± 1.1

Extended Data Figure 10 | See next page for caption.

**Extended Data Figure 10 | Verification of previous luminescence ages and inter-laboratory comparison.** **a**, Schematic diagram of square B4 (modified after ref. 13) showing the relative positions of four samples for which ages have been reported previously<sup>13,15,16</sup> and that were re-measured and evaluated in this study. **b–e**, Radial plots of single-grain  $D_e$  values measured in this study for these four samples. **b**, KTL165; **c**, KTL164; **d**, KTL158; **e**, KTL162. The grey bands in each plot are centred on the weighted mean  $D_e$  determined for each dose population using the central age model, after the rejection of outliers (shown as open triangles). **f**, Previously published  $D_e$  values, total dose rates and ages, together with the revised dose rates and ages (values in parentheses; see Supplementary Information for explanation) and the new single-grain OSL  $D_e$  values (based on the data shown in **b–e**) and ages obtained in this study. **g–j**, Radial plots of single-grain  $D_e$  values for the four samples measured independently in two laboratories (University of Wollongong,

UOW; University of Adelaide, UA). **g**, Sample 1 (SW13A); **h**, Sample 2 (SW11A); **i**, Sample 3 (SW7A); **j**, Sample 4 (SW5A). Filled circles and open triangles are  $D_e$  values obtained at UA and UOW, respectively. The grey bands in each plot are centred on the weighted mean  $D_e$  determined using the central age model for each dose population measured at UA. **k**, Comparison of weighted mean  $D_e$  and overdispersion (OD) values for the same samples measured at UA and UOW ('A') using a preheat combination of 260 °C for 10 s (PH<sub>1</sub>) and 220 °C for 0 s (PH<sub>2</sub>), and at UOW ('B') using a preheat combination of 220 °C for 10 s (PH<sub>1</sub>) and 160 °C for 5 s (PH<sub>2</sub>). **l**, High-resolution gamma-ray spectrometry results obtained at UA and the beta and gamma dose rates and OSL ages calculated from these data, compared to the beta and gamma dose rates and OSL ages obtained independently at UOW (using preheat combination 'A' for  $D_e$  determination).